



## Rat swarm political optimizer based deep learning approach for lung lobe segmentation and lung cancer detection using CT images



N. Velmurugan<sup>a,\*</sup>, R. Rajeswari<sup>b</sup>, Satuluri Naganjaneyulu<sup>c</sup>, A. Anupama<sup>d</sup>

<sup>a</sup> Department of Information Technology, Saveetha Engineering College, Thandalam, Chennai, Tamil Nadu 602105, India

<sup>b</sup> Department of Electronics and Communication Engineering, Rajalakshmi Institute of Technology, Chennai, Tamil Nadu, India

<sup>c</sup> Department of Information Technology, Lakireddy Balaji College of Engineering (Autonomous), Mylavaram, Andhra Pradesh 521230, India

<sup>d</sup> Department of Computer Science and Engineering, GITAM School of Technology, GITAM, Visakhapatnam, Andhra Pradesh, India

### ARTICLE INFO

#### Keywords:

Shepard Convolutional Neural Networks (ShCNN)  
Pyramid Scene Parsing Network (PSPNet)  
Deep Learning (DL)  
Political Optimizer (PO)  
Rat Swarm Optimizer (RSO)

### ABSTRACT

Lung lobe segmentation and lung cancer detection are crucial areas in medical imaging and diagnostics. Lung lobe segmentation helps in accurately identifying and analyzing specific regions of the lungs. The goal of lung cancer detection is to identify malignant tumors in the lungs at an early stage. Many methods exist for detecting lung cancer, but slow convergence and poor exploration affect the performance of these methods. Hence, in this research, the Rat Swarm Political Optimizer (RSPO) based Shepard Convolutional Neural Networks (ShCNN) is developed for lung cancer detection. The proposed RSPO is a combination of Rat Swarm Optimizer (RSO) and Political Optimizer (PO). Here, the input Computed Tomography (CT) image is taken from the database. After that, this input is fed towards the pre-processing stage. The pre-processing is done using a Laplacian filter and the pre-processed image is allowed for lung lobe segmentation. Here, the lung lobe segmentation is done using Pyramid Scene Parsing Network (PSPNet) which is trained by the proposed RSPO. Further, nodule identification is carried out by a grid-based scheme. Following this, the feature extraction is performed to extract the relevant features. At last, the extracted features are allowed towards lung cancer detection using the developed RSPO\_ShCNN. Moreover, the RSPO\_ShCNN's performance is evaluated by accuracy, F-measure, as well as precision. The RSPO\_ShCNN achieves high values of accuracy, precision and F-measure as 0.948, 0.926, and 0.937. Furthermore, the accuracy of the proposed RSPO\_ShCNN is 19.51 %, 15.08 %, 1.66 % and 4.11 % higher than the traditional methods.

### 1. Introduction

In the world, Carcinoma is the leading disease that causes death. Carcinomas are termed as cancers starting in the cells, which grow up on the tissue lining organs or skin, like lungs or kidneys. Carcinoma of the lungs or lung cancer is characterized by unrestricted cell growth in lung tissue and characterized by a particular pattern of growth [1]. Lung cancer is a major cause of death in the world wide context. In the year 2018, pulmonary cancer caused 142, 670 deaths alone in the United States (US) [2 3]. People diagnosed with lung cancer are above the age of 65 years, and there is a very small number of people below 45 years diagnosed with this lung cancer [4]. Lung cancer is a crucial disease to be untreated, as this propagates to parts of the body. Non-small cell lung carcinoma is a main kind, and the primary reason for this lung cancer is smoking. Lung cancer is also found in many people with no smoking

history but with exposure to secondary smoking, air pollution, and sometimes gasses that are toxic [1]. Nodules present in lungs allude to variations in lung tissue from the norm, which is generally circular fit as a fiddle of dimensional width of 3 mm as well as 30 mm [5]. Any influenced locale below 3 mm is called a miniaturized scale nodule, and anything prominent than 30 mm is called a mass [6]. This sort of nodule is probably going to be cancerous and should be considered at the right time [7].

The usage of retinal fundus images, CT scans, or other medical imaging modalities helps to identify, segment, and classify abnormalities or diseases [8 9]. Major diagnostic techniques for lung cancer include radiography and CT scan, bronchoscopy, imaging, and biopsy [4]. CT is a useful imaging technique that becomes more significant for lung nodule diagnosis and characterization. It is advantageous for chest radiography in relation to resolution. CT provides good resolution and it

\* Corresponding author.

E-mail address: [velmurugan@saveetha.ac.in](mailto:velmurugan@saveetha.ac.in) (N. Velmurugan).

is capable of concluding small as well as low-contrast nodules [10], which paves the way for earlier lung nodule detection. There are many research works in image processing methods at present, which concentrate on detecting automatically, segmenting, and assessing lung nodules gained using CT imagery [11]. On the other hand, the usage of CT images for assessing lung nodules needs to review a complex and large number of volumetric datasets [1213]. CT is a combination of X-rays acquired from various angles with combination processing to acquire pictures of exact parts of the body. Four stages are present in cancer in the lung, which is stage I, stage II, stage III, as well as stage IV. Stages I, II, as well as III are found by axial CT. Stage IV patients feel symptoms because cancer has spread through out the body and cannot be identified from a CT scan [14]. It is categorized as malignant from stage II on because of its high death rate (60–70 %) and hard-to-cure nature. Hence, earlier detection of lung cancer is needed to find whether cancer is malignant or not, so that treatment is done as soon as possible [15].

CT scans are done by radiologists for elements possibility as well as this is carried out slice manner that is considered to take more time. Computer Aided Diagnosis (CAD) eradicates many difficulties that radiologists face when caring. CAD aims to analyze malignant and non-malignant nodules or masses clearly with the help of suitable Machine Learning (ML) approaches [16]. A huge count of techniques is used in executing pulmonary nodule segmentation and is called thresholding technique, histogram-related segmentation, morphological technique, graph-cut model, clustering model, deformable method, Neural Networks (NN), region growing, as well as Markov Random Field (MRF). Besides, thresholding is the most familiar conventional segmentation method, although the performance of the thresholding scheme is not needed [11]. Most segmentation techniques use combined models and are mainly related to threshold with regional growth and other extraction models that rely on clustering techniques [13]. Detecting lung cancer is done earlier depending on algorithms related to image processing. Artificial Intelligence (AI) based methods are more efficient for medical tasks including detection and prediction of various diseases [17]. Previously, tumor diagnosis was related to ML and many statistical features including color, moment, geometry, as well as texture features. DL algorithms are becoming a technique to analyze medical images, mainly CNNs [18 19]. The new part of ML is DL which employs ordered constructions to learn high-level summaries of data and is developing procedure, which is used widely in medical imaging [4]. The performance of CNN is widely improvised, because of the development of Fully Convolutional Neural Networks (FCNs) [20]. Moreover, U-Net is one of the most efficient models of FCN during medical image segmentation [21].

### 1.1. Problem statement

Lung lobe segmentation involves dividing a lung image into its constituent lobes. Lung cancer detection aims to identify malignant nodules or tumors in the lungs. Lung lobe segmentation and lung cancer detection are both critical to appropriate diagnosis and therapy planning. Many lung cancers are discovered in an advanced stage, which reduces the effectiveness of treatment. Existing methods for lung lobe segmentation and lung cancer detection face several challenges:

- Variations in image quality due to different imaging protocols and equipment affect the segmentation accuracy.
- The intricate structure of the lungs and the presence of similar-looking tissues pose challenges in accurately segmenting the lobes.
- Slow convergence and poor exploration affect the performance of the traditional models.
- Detecting small nodules was difficult in the previous methods.
- High rates of false positives and negatives can lead to unnecessary anxiety or missed diagnoses.

Here, the Laplacian Filter is used for image preprocessing. It

enhances edge details and reduces noise which optimizes the quality of the image. Then, the lung lobe segmentation is performed by the PSP Net, which is trained by the invented RSPO. The use of PSP Net allows for better handling of complex lung structures. It effectively captures both local and global features which enhances segmentation accuracy, especially in the presence of irregularities in the lung boundaries or regions with overlapping anatomical features. Moreover, the RSPO is a hybridization of RSO and PO. Here, the RSO converges quickly to the optimal solution, making it efficient for real-time applications. On the other side, the PO achieves faster convergence and better exploration capabilities. After that, a grid-based scheme is employed for nodule identification, allowing for more precise localization of potential tumor regions. It divides the image into smaller regions for detailed analysis, which improves the detection of small nodules. Following this, the relevant features are extracted in the feature extraction phase. Finally, lung cancer detection is carried out by the developed RSPO ShCNN. ShCNN is robust to variations in image quality and noise, ensuring reliable performance even with imperfect data. The use of RSPO avoids local minima and fine-tunes the ShCNN model's parameters to improve overall detection accuracy, reducing false positives and negatives. Hence, the invented approach differs from and improves upon these established previous works.

### 1.2. Contribution

The major contributions is,

- **RSPO\_ShCNN for lung cancer detection:** The ShCNN is designed for the detection of lung cancer. Here, the proposed RSPO is used to tune the ShCNN, which is formed by a combination of PO and RSO.
- **RSPO\_PSPNet for lung lobe segmentation:** The RSPO-based PSP Net is introduced for lung lobe segmentation. The PSP Net is trained by the RSPO.

The remaining parts as follows: **Section 2** indicates the motivation, literature assessment, as well as challenges of present papers related to lung cancer detection, and **Section 3** includes about full proposed system utilized for lung cancer detection. **Section 4** represents the results as well as the discussion. **Section 5** concludes the paper.

## 2. Motivation

Some lung cancers are identified by screening, but most lung cancers are identified due to the problems caused by them. An actual lung cancer diagnosis is made by analyzing a sample of lung cells in the lab. CT scan is more likely to show tumors of the lung than routine chest X-rays. This shows the size, position, as well as shape of lung tumors and helps in finding enlarged lymph nodes containing cancer. Even though there are several methods for determining lung cancer, early detection of cancer is not possible and hence DL-based method helps to eradicate the above issue.

### 2.1. Literature assessment

Althubiti, S.A., et al. [1] used Ensemble Learning Framework with Gray-Level Co-occurrence Matrix Texture (GLCM) for earlier detection of lung cancer on CT images. This model was good at performing segmentation with higher accuracy and reduced time. However, the analysis as well as modelling were not powerful enough for larger datasets. Masood, A., et al. [3] developed a Multidimensional Region-based Fully Convolutional Network (mRFCN) for lung cancer detection and classification. This system not only indicated nodule presence but also gave the location and outlined shape of the detected nodule. However, it did not have the accurate construction of testing or training sets, which led to lower performance classification. Niyaz Ahmad Wani., et al. [4] devised Deep Xplainer for lung cancer detection. This solution relied on

**Table 1**  
Review of the literature survey.

Reference	Methods	Preprocessing techniques	Type of dataset	Evaluation measures	Advantages	Disadvantages
Althubiti, S.A., et al. [1]	GLCM	mean, median, Gaussian and 2D convolution	—	Accuracy, True positive (TP), True negative (TN), False positive (FP) and False negative (FN).	This method was good at performing segmentation with higher accuracy and reduced time.	The analysis as well as modelling was not powerful enough for larger datasets.
Masood, A., et al. [3]	mRFCN	—	LIDC-IDRI, Clinical Dataset	Sensitivity, Standard Deviation Detection Error Rate, FP per section, FP per case, Mean ANODE (mAN) Score and processing time.	It gave the location and outlined shape of the detected nodule.	However, it did not have the accurate construction of testing or training sets, which led to lower performance classification.
Niyaz Ahmad Wani, et al. [4]	DeepExplainer	—	Survey Lung Cancer dataset	Accuracy, sensitivity, F1-score	It made the predictions with high accuracy.	However, biased data led to inaccurate predictions.
Jena, S.R. and George, S. T., [22]	KNG-CNN	ROI extraction	LIDC-IDRI	Accuracy, precision, F-measure and recall	This method guaranteed faster convergence with better results and was efficient to avoid overfitting.	However, this technique had poor generalization.
Nanglia, P., et al. [11]	FFBP-NN	—	—	Sensitivity and accuracy	This technique produced minimal error even in the presence of noise,	This technique did not include variation in the fitness function to improve efficiency.
Rajan Baby, Y. and Ramayyan Sumathy, V.K., [13]	BFC	fuzzy median filter	Lung Image Database Consortium image (LIDC-IDRI)	Accuracy, False positive rate (FPR), Specificity, Jaccard coefficient and Dice coefficient.	Smaller and medium-term irregularities were efficiently processed using Kernel-BFC, leading to superior results.	However, this technique needed higher processing time.
Veronica, B.K., et al. [7]	ANN with OALO	ROI extraction	ELCAP public lung image database, LIDC/IDRI Database and Marthandam Lung CT scan images	Sensitivity, specificity and accuracy	This method required minimal computational time.	Failed to improve accuracy by extracting features of lung images.
Tiwari, L., et al. [16]	TWEDLNN	—	LIDC-IDRI database	Recall, sensitivity, F-measure, Negative Predictions Value (NPV), specificity, precision, FNR, accuracy, FPR, MCC and False Rejection Rates (FRR).	This technique was effective in producing minimal misclassifications	It was difficult to identify the small nodules.
M.Navaneethakrishnan., et al. [23]	BDHOA-based DCNN	—	LIDC-IDRI repository	Accuracy, sensitivity, and specificity	This model helped to fine-tune the parameters and led to better performance.	However, this model had high training and inference time.
Lavina Jean Crasta., et al. [24]	DL framework	resizing, intensity normalization, and truncation of image values.	LUNA16 dataset	Accuracy, specificity, sensitivity and F1-Score	This model identified the suspicious regions in small nodules and aided in early diagnosis.	However, it was computationally expensive and time-consuming.
Proposed method	RSPO_ShCNN	Laplacian filter	LIDC-IDRI dataset and Medical Deepfakes: Lung Cancer dataset	Accuracy, F1 measure, and precision	Converges quickly to the optimal solution effectively captures both local and global features, has better exploration capabilities, robust to variations in image quality and noise and avoids local minima.	—

a convolutional neural network and XGBoost. XGBoost was used to predict class labels after 'Deep Explainer' learned the input's features via its multiple convolutional layers. To provide explanations or explainability of forecasts, an explainable artificial intelligence method known as 'SHAP' was employed. It made the predictions with high accuracy. However, biased data led to inaccurate predictions. Jena, S.R. and George, S.T., [22] introduced a Kernel-based Non-Gaussian Convolutional Neural Network (KNG-CNN) for early lung cancer detection. This method guaranteed faster convergence with better results and was efficient to avoid over fitting. However, this technique had poor generalization.

Nanglia, P., et al. [11] designed Feed Forward Back Propagation Neural Network (FFBP-NN) for lung cancer categorization. This technique produced minimal error even in the presence of noise, but this

technique did not include variation in the fitness function to improve the efficiency. Rajan Baby, Y. and Ramayyan Sumathy, V.K., [13] used Kernel- Bayesian Fuzzy Clustering (BFC) for lung nodule segmentation. Smaller and medium-term irregularities were efficiently processed using Kernel-BFC, leading to superior results. However, this technique needed higher processing time. Veronica, B.K., et al. [7] developed Artificial Neural Network (ANN) with Oppositional-based Ant Lion Optimization (OALO) for lung nodule detection in CT images. This method required minimal computational time, but this technique failed to improve accuracy by extracting features of lung images. Tiwari, L., et al. [16] introduced Target based Weighted Elman DL Neural Network (TWEDLNN) for the detection of lung nodules and cancer. This technique was effective in producing minimal misclassifications, but in this technique was difficult to identify the small nodules.M.

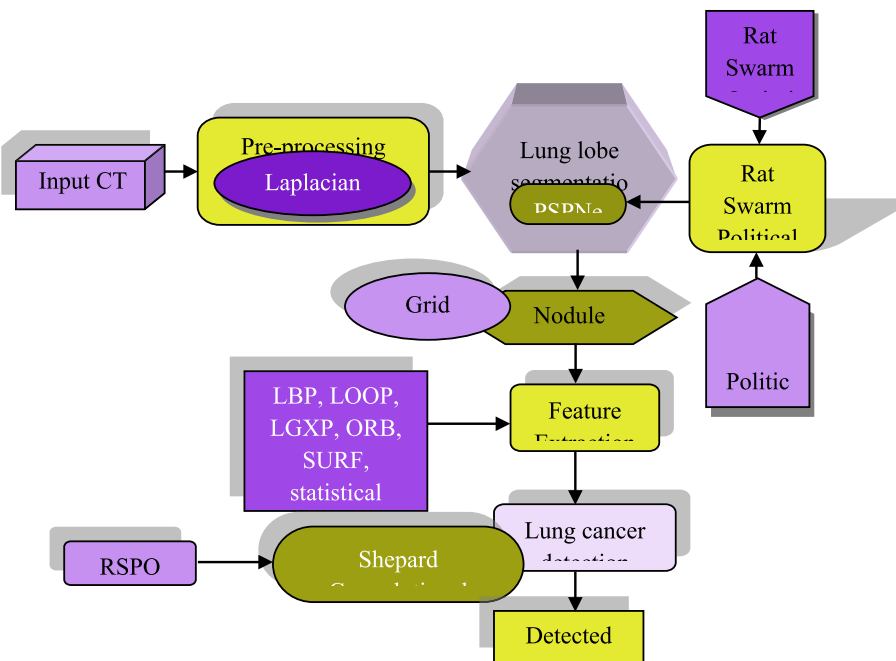


**Fig. 1.** Diagram of RSPO\_ShCNN for lung cancer detection using CT images.

Navaneethakrishnan., et al. [23] devised a Bat Deer Hunting Optimization Algorithm-based Deep Convolutional Neural Network (BDHOA-based DCNN). Here, the Deep Fuzzy SegNet was used for lung nodule region segmentation, which identified the accurate lung nodule location. The BDHOA-based DCNN classified the lung cancers based on the segmented regions. This model helped to fine-tune the parameters and led to better performance. However, this model had high training and inference time. Lavina Jean Crasta., et al. [24] devised a DL framework to classify and detect lung cancer in input CT images. Here, the 3D-VNet architecture was used to segment the pulmonary nodule and D-ResNet architecture was utilized for classification. This model identified the suspicious regions in small nodules and aided in early diagnosis. However, it was computationally expensive and time-consuming. Table 1 shows the review of the literature survey.

## 2.2. Research gaps

Challenges faced by existing techniques for lung cancer detection are described as follows,

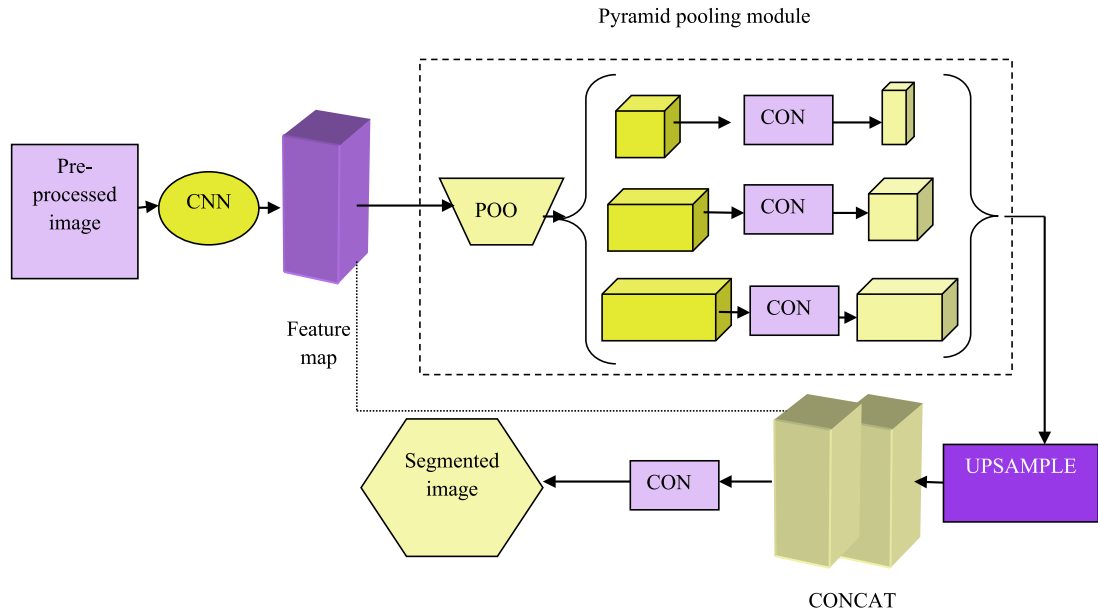
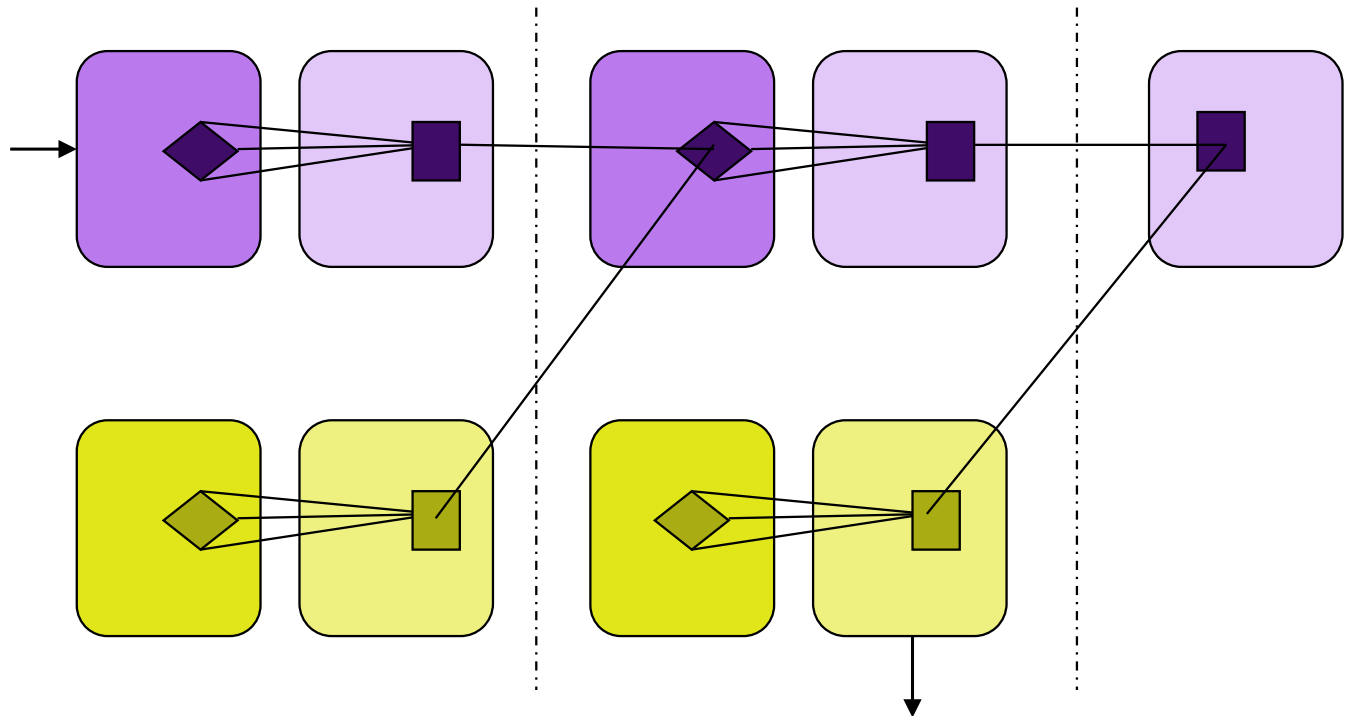
- In [3], an mRFCN-based automated decision support system was devised for lung cancer detection that automatically selected potential Region-of-Interest. However, it failed in focussing on detecting micro nodules, at which the diameter is less than 3 mm to enable the system to work well with every kind of nodules when maintaining performance.
- KNG-CNN was devised for lung cancer detection in [22] and this algorithm ensured accurate prediction of lung nodules with reduced computational overhead. Moreover, this technique failed to include a platform of big data having hybrid datasets for performance improvement.
- Kernel-BFC developed for lung cancer detection in [13] applied to real-world problems, but it failed in choosing a Gaussian smoothed image depending on the scale of key points.
- In [16], TWEDLNN was developed and this was relatively simple and produced more accurate and sophisticated classification results, but this technique required along time for network training and sometimes network may not converge at all.

- Many works have been devised for classifying lung cancer and the limitation of models was a dependency on the image as well as an inability to detect nodules overlapping anatomic structures. Furthermore, the visible presence of deviations in nodules and the variety of nodules within the lungs provide challenges to the accuracy of lung nodule segmentation. Therefore, it is necessary to segment lung nodules efficiently.

In this paper, the RSPO\_PSPNet is developed for lung lobe segmentation and the RSPO\_ShCNN is invented for lung cancer detection. Initially, the preprocessing is done by the Laplacian filter. Then, the lung lobe segmentation is performed by PSP Net, which is trained by a RSPO. After that, the grid-based scheme is used for the identification of nodules. Then, the relevant features are extracted by performing the feature extraction. Finally, lung cancer is detected using the developed RSPO\_ShCNN.

## 3. RSPO\_ShCNN for lung cancer detection

Lung cancer is a cancer type beginning in the lungs. This cancer doesn't cause any signs in earlier stages and lung cancer symptoms occur when the disease becomes advanced. The main objective is to develop novel methods such as RSPO\_PSPNet for lung lobe segmentation and RSPO\_ShCNN for lung cancer detection. The diagram of the proposed RSPO\_ShCNN for lung cancer detection by using CT images is displayed in Fig. 1. First, a sample of an input CT image is obtained from two databases as LIDC-IDRI dataset and the Medical Deepfakes: Lung Cancer dataset. Then, the input image is preprocessed by using the Laplacian filter. After that, lung lobe segmentation is performed by the PSPNet, which is trained by the proposed RSPO. Moreover, the RSPO is an integration of RSO and PO. Following this, a grid-based method is employed for nodule identification. Next, the feature extraction process is done to extract the features such as Oriented Fast and Rotated BRIEF (ORB), Local Binary Pattern (LBP), Local Optimal Oriented Pattern (LOOP), Local Gabor XOR Patterns (LGXP), and Speeded Up Robust Feature (SURF), as well as statistical features like kurtosis, variance, mean, standard deviation, and skewness. Finally, the proposed RSPO\_ShCNN performs lung cancer detection.

**Fig. 2.** Diagram of PSP Net.**Fig. 3.** Diagram of ShCNN.

### 3.1. Acquisition of image

Here, image is acquired from the Lung Image Database Consortium image collection (LIDC-IDRI) dataset [25] and the Medical Deepfakes: Lung Cancer dataset [26] which has many CT images. The dataset is indicated as below,

$$P = \{P_1, P_2, \dots, P_c, \dots, P_d\} \quad (1)$$

where, the dataset with many CT images is represented as  $P$ ,  $P_c$  indicates  $c^{th}$  CT image used as input for pre-processing, and  $P_d$  is  $d$  number of CT images in the database, which represents the full number of images.

### 3.2. Pre-processing by Laplacian filtering

The input image  $P_c$  is allowed for the pre-processing phase, which is carried out by Laplacian filtering [27]. Laplacian filter highlights the input image by removing noise and enhances the image. Here, the Laplacian operator  $\Delta^2$  is indicated by,

$$\Delta^2 = \frac{\partial^2 v}{\partial^2 x^2} + \frac{\partial^2 v}{\partial^2 y^2} \quad (2)$$

where,  $v(x,y)$  indicates image. the pre-processed image is indicated as  $L_c$ , which is fed for next step.

*i) Experimental results of normal CT images*

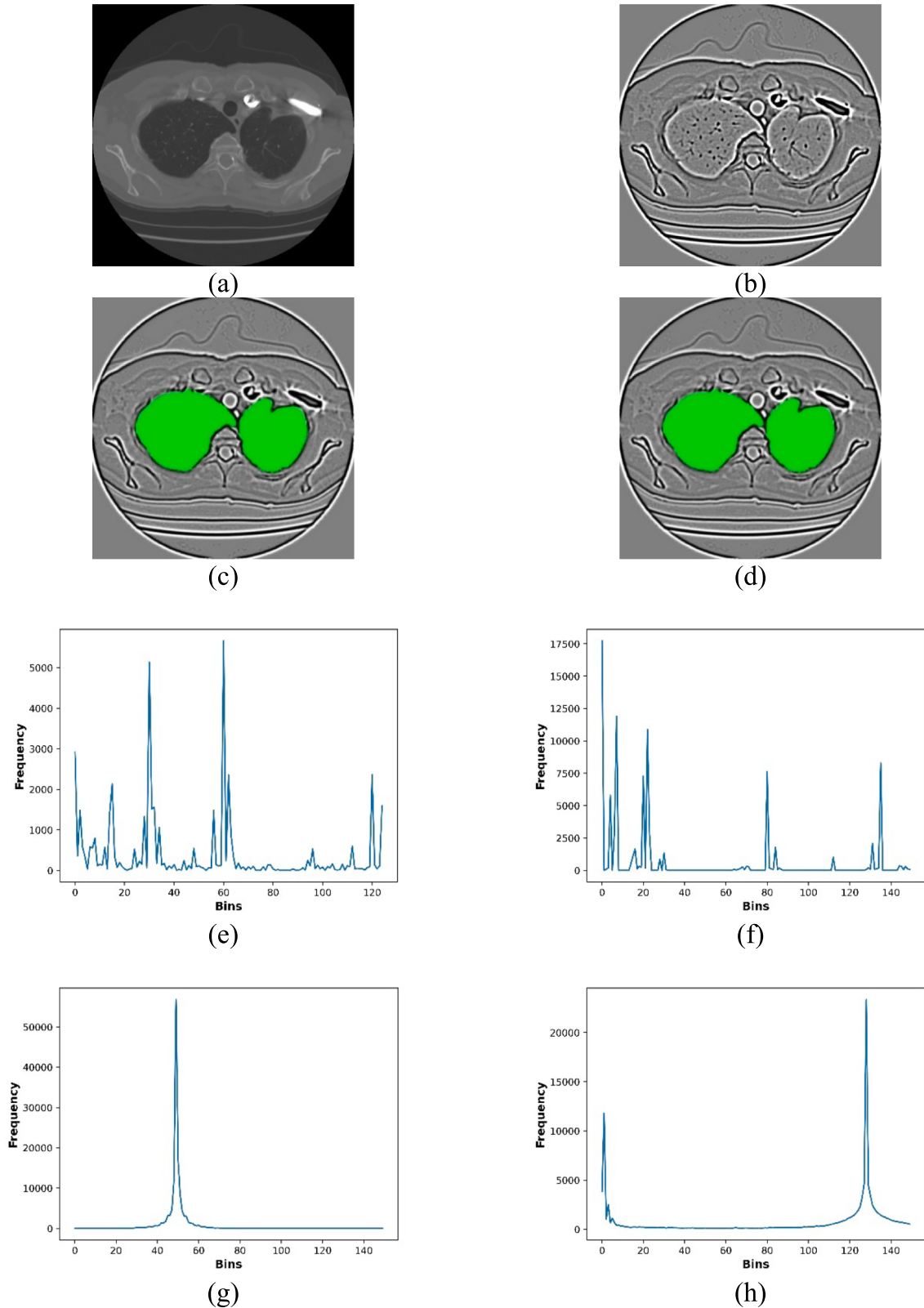


**Fig. 4.** Experimental results of normal CT images a) input, b) processed, c) lobe segment, d) nodule segment, e) LBP extracted, f) LOOP extracted, g) LGXP extracted, h) ORB extracted and i) SURF extracted images.

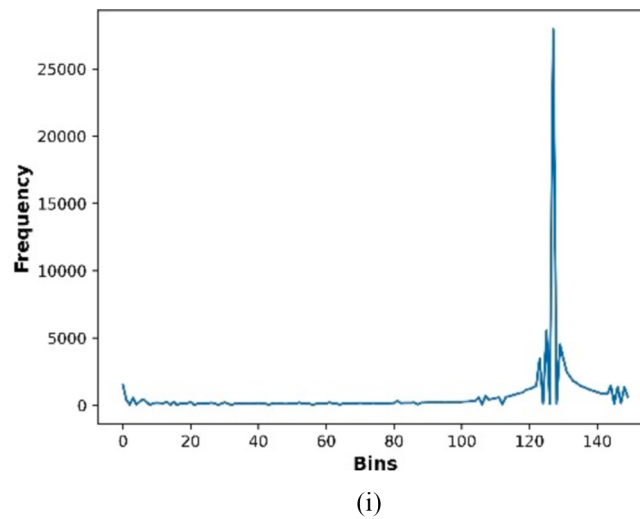


Fig. 4. (continued).

### 3.3. Lung lobe segmentation using PSP Net

Lung lobe segmentation is carried out by PSP Net [28], at which a pre-processed image is taken as input. PSP Net converts images into a collection of pixel regions. By segmenting the image, the key areas are identified and made suitable for the nodule identification process. Here, PSP Net helps in segmenting the lung lobe area.

#### 3.3.1. PSP Net architecture

Fig. 2 indicates PSP Net architecture for lung lobe segmentation. PSP Net [28] helps in the segmentation module at which pixels in the image are annotated. The pyramid pooling module includes elements from four different pyramid scales. The outcome of the pyramid pooling module's multiple layers produces feature maps of varying sizes. After each pyramid level, the convolution layer  $1 \times 1$  is used to reduce the context representation dimension to  $1/A$  of the original one, if the pyramid level size is A, in order to retain global feature weight. Then, up sampling is carried out on low-dimension feature maps to utilize bilinear interpolation and gain the original feature map. Lastly, a final pyramid pooling global feature is created by concatenating many feature levels. The output gained from PSP Net is indicated by  $M_c$ .

#### 3.3.2. RSPO for PSP Net training

PSP Net is the DL model that is trained by RSPO for lung lobe segmentation. Here, RSPO is the combined optimization algorithm of RSO [29] and PO [30]. In the optimization challenges, RSO has great precision. This accuracy can be crucial for identifying cancerous cells in medical images. It exhibits fast convergence, which helps to timely diagnoses and better patient outcomes. Also, it has fewer parameters which gives better computational efficiency and reduces memory usage. PO is a global optimization algorithm inspired by a multi-phased political system. PO efficiently handles multi-class classification tasks. It allows the model to distinguish between benign nodules and malignant tumors efficiently. The PO uses gradient descent during training. This facilitates the model to effective convergence toward the ideal solution. So the integration of these two models provides better results.

Both PO and RSO get combined in forming RSPO that helps in solving highly constrained problems. Algorithmic procedure of RSPO is indicated below,

### 4. Rat swarm position encoding

The better solution is found in search space X, in which PSP Net's learning parameter is resembled by  $\alpha$ . It is denoted by  $X = [1 \times \alpha]$ .

### 5. Finding fitness

Calculating fitness is done by the below equation to enable optimal solutions to solve design complexity and imbalanced conflict issues of optimization. This function utilizes the results attained from PSP Net as well as targeted output and is formulated as,

$$Fs_1 = \frac{1}{d} \sum_{c=1}^d [Tar_c^* - M_c]^2 \quad (3)$$

where,  $Fs_1$  is fitness term based on PSP Net output,  $d$  is total images,  $M_c$  is output gained from PSP Net, and  $Tar_c^*$  is targeted output.

#### Step 1: Initialization

Rats are tiny-size das well as longer-tailed rodents that differ based on weight and size. There are dual rat species like brown and black rat. In the family of rats, males are termed bucks and females are termed does. RSO is initialized with a population of rats in the search agent, which is indicated as,

$$B_j (j = 1, 2, \dots, r) \quad (4)$$

#### Step 2: Fitness evaluation

Fitness is determined by finding the maximal optimum solution that yields the best solution, and this is indicated in above Eq. (3).

#### Step 3: Chasing prey

Rats chase prey via social agonistic habit. Here, the best search agent shows knowledge of locating prey. Additionally, the top search agent positions are updated by other search agents, which is represented as,

$$\vec{B} = P \cdot \vec{B}_j(a) + R \cdot \left( \vec{B}_s(a) - \vec{B}_j(a) \right) \quad (5)$$

where, the position of rats is indicated as  $\vec{B}_j(a)$ , and the best optimum solution is represented as  $\vec{B}_s(a)$ . Here, the parameters  $P$  and  $R$  are given as,

$$P = K - a \times \left( \frac{K}{Max_{iter}} \right) \quad (6)$$

where,  $a = 0, 1, 2, \dots, Max_{iter}$

$$R = 2.rand() \quad (7)$$

where,  $K$  and  $R$  are random numbers between [1, 5] and [0, 2]. Parameters  $P$  as well as  $R$  are responsible for best exploration as well as exploitation over iterations.

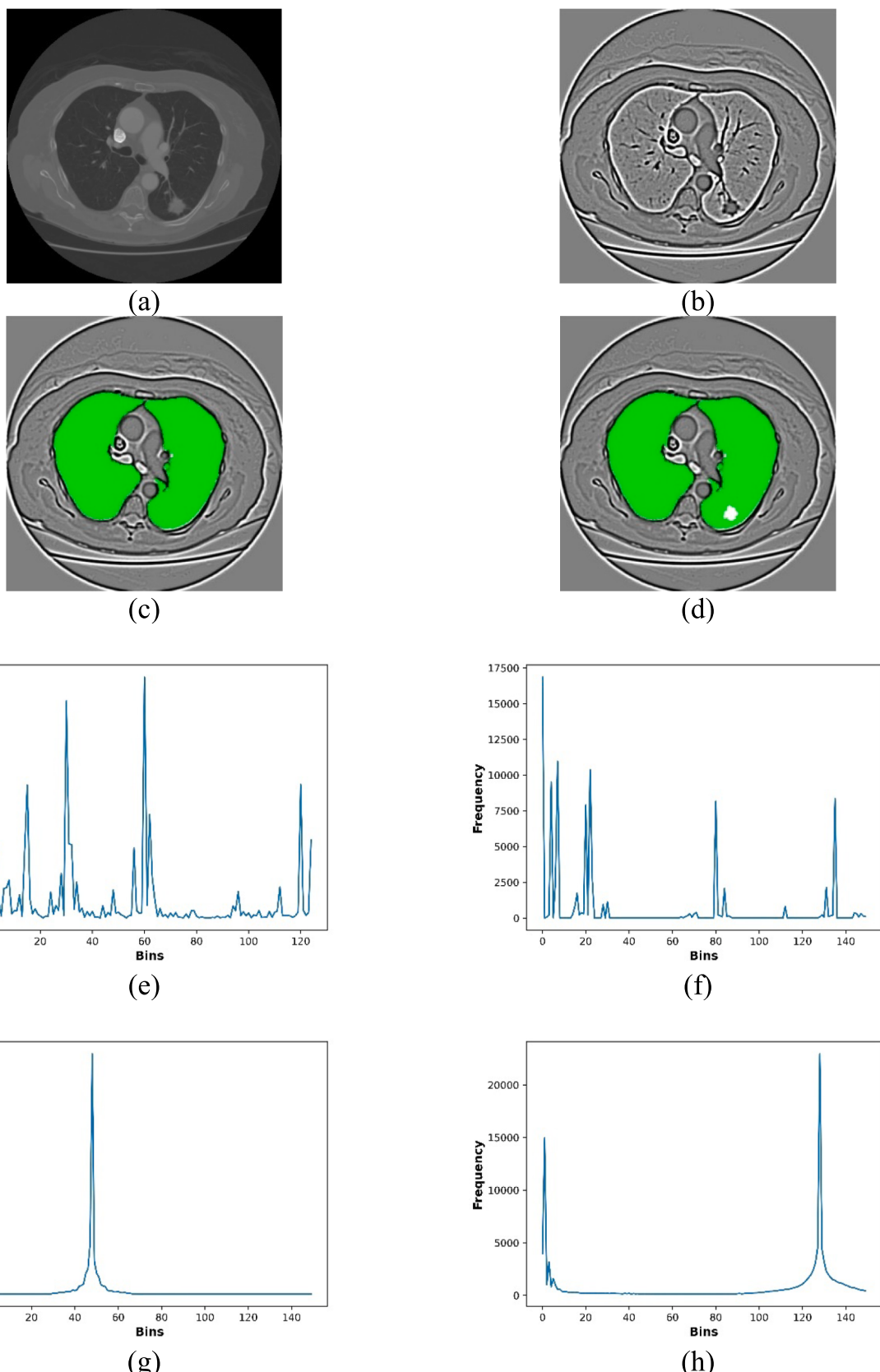
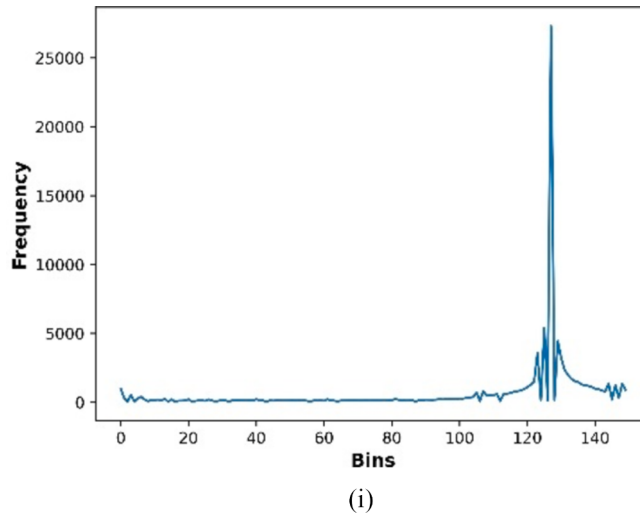


**Fig. 5.** Experimental results of cancerous CT images a) input, b) processed, c) lobe segment, d) nodule segment, e) LBP extracted, f) LOOP extracted, g) LGXP extracted, h) ORB extracted and i) SURF extracted images.



(i)

Fig. 5. (continued).

**Step 4: Fighting with prey**

Rats fight with prey and this is indicated in below equation,

$$\vec{B}_j(a+1) = \left| \vec{B}_s(a) - \vec{B} \right| \quad (8)$$

where,  $\vec{B}_j(a+1)$  is updated next position of therat. Assume,  $\vec{B}_s(a) > \vec{B}$ ,

$$\vec{B}_j(a+1) = (\vec{B}_s(a) - \vec{B}) \quad (9)$$

By substituting Eq. (5) in Eq. (9) it becomes,

$$\vec{B}_j(a+1) = \vec{B}_s(a) - P \cdot \vec{B}_j(a) - R \cdot \vec{B}_s(a) + R \cdot \vec{B}_j(a) \quad (10)$$

$$\vec{B}_j(a+1) = \vec{B}_s(a)[1-R] + \vec{B}_j(a)[R-P] \quad (11)$$

The basic equation of PO is given as,

$$\begin{aligned} h_{j,q}^p(w+1) &= h_{j,q}^p(w-1) + l(h_{j,q}^p(w) - h_{j,q}^p(w-1)), \text{ if } h_{j,q}^p(w-1) \leq t^* \\ &\leq h_{j,q}^p(w) \text{ (or) } h_{j,q}^p(w-1) \geq t^* \geq h_{j,q}^p(w) \end{aligned} \quad (12)$$

here,  $h_{j,q}^p(w+1) = \vec{B}_j(a+1)$ ,  $h_{j,q}^p(w-1) = \vec{B}_j(a-1)$ , and  $h_{j,q}^p(w) = \vec{B}_j(a)$

Then, Eq. (12) becomes,

$$\vec{B}_j(a+1) = \vec{B}_j(a-1) + l(\vec{B}_j(a) - \vec{B}_j(a-1)) \quad (13)$$

$$\vec{B}_j(a) = \frac{\vec{B}_j(a+1) - \vec{B}_j(a-1)(1-l)}{l} \quad (14)$$

Substitute Eq. (14) in Eq. (11) indicating hybridization of PO with RSO,

$$\vec{B}_j(a+1) = \left( \frac{\vec{B}_j(a+1) - \vec{B}_j(a-1)(1-l)}{l} \right) [R-P] + \vec{B}_s(a)[1-R] \quad (15)$$

$$\vec{B}_j(a+1) - \frac{\vec{B}_j(a+1)}{l}[R-P] = \left( \frac{\vec{B}_j(a-1)(l-1)}{l} \right) [R-P] + \vec{B}_s(a)[1-R] \quad (16)$$

$$\frac{\vec{B}_j(a+1)l - \vec{B}_j(a+1)[R-P]}{l} = \frac{-\vec{B}_j(a-1)(l-1)[R-P] + \vec{B}_s(a)[1-R]l}{l} \quad (17)$$

$$\vec{B}_j(a+1)(l-R+P) = -\vec{B}_j(a-1)(l-1)[R-P] + \vec{B}_s(a)[1-R]l \quad (18)$$

$$\vec{B}_j(a+1) = \frac{\vec{B}_s(a)[1-R]l - \vec{B}_j(a-1)(l-1)[R-P]}{(l-R+P)} \quad (19)$$

where, the best solution is  $\vec{B}_s(a)$ ,  $j^{th}$  solution position at  $(a-1)^{th}$  iteration is  $\vec{B}_j(a-1)$ . The above equation represents the basic equation of RSPO to train PSP Net.

**Step 5: Termination**

The procedure is repeated until the maximal optimal solution for PSP Net training is obtained, which is determined by the fitness equation in Eq. (3). The pseudocode of RSPO is depicted in Algorithm 1.

**Algorithm 1. (Pseudo code of RSPO)**

S. No.	Pseudo code of RSPO
1	<b>Input:</b> Rats population $\vec{B}_j(j = 1, 2, \dots, r)$
2	<b>Output:</b> Optimal solution $\vec{B}_j(a+1)$
3	<b>Start RSPO</b>
4	Initializing parameters $P, R, K$
5	Using Eq. (33) to find the fitness function.
6	Find the best search agent $\vec{B}_s$
7	<b>while</b> ( $a < \text{Max}_{\text{iter}}$ ) <b>do</b>
8	<b>for all</b> search agents <b>do</b>
9	The current search agent's position is updated using Equation (8)
10	<b>end for</b>
11	<b>Hybridization of PO with RSO,</b>
12	The basic equation of RSPO is given by Eq. (19)
13	Update parameters $P, R, K$
14	Check if there is any search agent that goes beyond the given search space and adjust it
15	Update $\vec{B}_s$ if there is a better solution than the optimum solution
16	$a \leftarrow a + 1$
17	<b>end while</b>
18	<b>return</b> $\vec{B}_s$
19	Reevaluate by fitness function by Eq. (33)
20	Find the best solution
21	<b>End RSPO</b>

### 5.1. Identification of nodules by grid-based scheme

Following lung lobe segmentation, a grid-based technique is used to identify the nodule. Segmented image  $M_c$  is allowed for nodule seg-

mentation. This scheme identifies whether the nodule region is affected by disease. In this case, the segmented lung lobes  $M_c$  are divided into several blocks called grids using this approach. This is required for splitting segmented images into several blocks in order to simplify

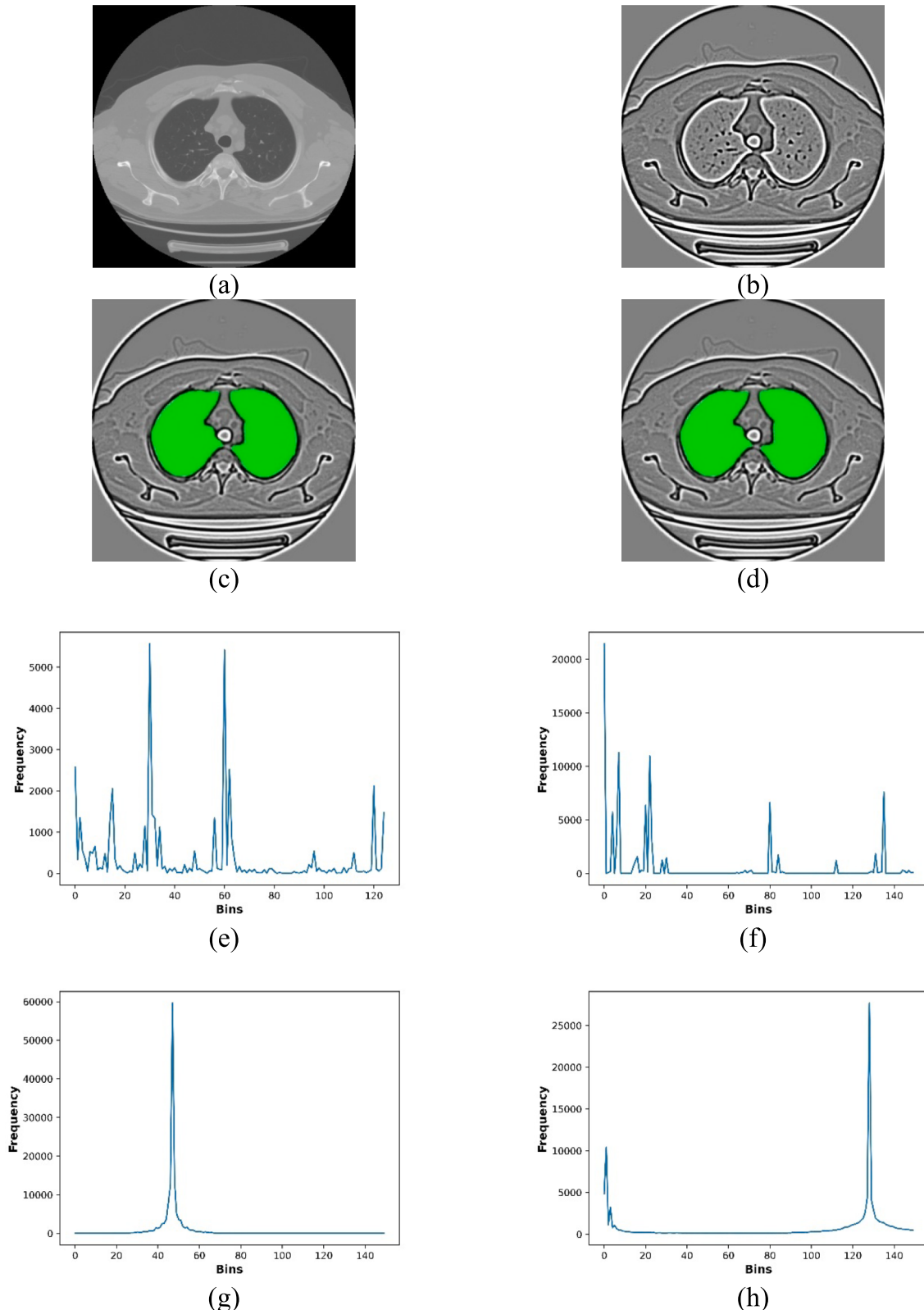


**Fig. 6.** Experimental results of normal CT images a) input, b) processed, c) lobe segment, d) nodule segment, e) LBP extracted, f) LOOP extracted, g) LGXP extracted, h) ORB extracted and i) SURF extracted images.

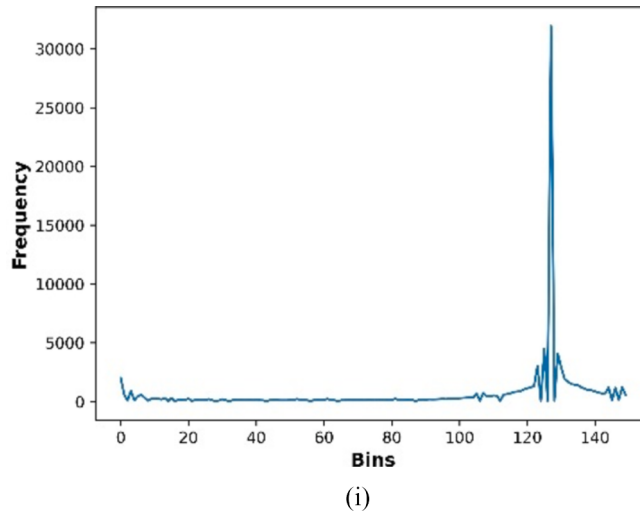


Fig. 6. (continued).

computations and shorten computation times. The segmented region is split into multiple grids using a grid-based method in order to detect lung nodules. As a result, the segmented image's nodule region is identified and denoted as  $D_c$ .

## 5.2. Feature extraction

After completion of nodule identification  $D_c$ , features get extracted. Here, features extracted include statistical features such as standard deviation, skewness, variance, kurtosis as well as mean, wherein other features extracted are LBP, LOOP, LGXP, ORB, as well as SURF.

**a) LBP:** LBP [31] is a local image texture that is utilized everywhere as a simple feature. This is represented as  $3 \times 3$  neighborhoods which, based on the neighborhood pixels surrounding the middle one, provide 8-bit codes. LBP provides severe alterations over-illumination and is indicated as,

$$LBP(f_c, g_c) = \sum_{e=0}^7 m(o_u - o_c)2^e \quad (20)$$

Here, the function  $m(x)$  is indicated by,

$$m(x) = \begin{cases} 1, & \text{if } x \geq 0 \\ 0, & \text{if } x < 0 \end{cases} \quad (21)$$

where,  $o_u$  and  $o_c$  are grey level values of surrounding pixels and central pixel, and  $e$ , 8neighbours of the central pixel. Thus, LBP is indicated by term  $F(1)$ .

**b) LOOP:** LOOP [31] is an non-linear incorporation of local Directional Pattern (LDP) and LBP. LOOP is generated to overcome the drawbacks of both LDP as well as LBP. The LOOP is indicated as,

$$LOOP(f_c, g_c) = \sum m(o_u - o_c)2^z \quad (22)$$

Here,

$$m(x) = \begin{cases} 1, & \text{if } x \geq 0 \\ 0, & \text{otherwise} \end{cases} \quad (23)$$

As a result, rotation invariance denoted by  $F(2)$  is found by LOOP.

**c) LGXP:** In LGXP [32], phases are quantized into various ranges, and then the LXP operator is applied to quantized phases of the central pixel as well as each of its neighbors. Finally, the middle pixel's local pattern is created by integrating the binary labels. Thus, LGXP in decimal and binary are indicated by,

$$LGXP_{\beta,\chi}(v_A) = [LGXP_{\beta,\chi}^B, LGXP_{\beta,\chi}^{B-1}, \dots, LGXP_{\beta,\chi}^1]_{\text{binary}} \quad (24)$$

$$LGXP_{\beta,\chi}(v_A) = \left[ \sum_{b=1}^B 2^{b-1} \cdot LGXP_{\beta,\chi}^b \right]_{\text{decimal}} \quad (25)$$

where, middle pixel location with orientation  $\beta$  and  $\chi$  scale in the Gabor phase map, neighborhood size is  $B$ , as well as  $LGXP_{\beta,\chi}^b$  ( $b = 1, 2, \dots, B$ ) indicates pattern calculated among  $v_A$  and  $v_b$  that is calculated as below,

$$LGXP_{\beta,\chi}^b = \delta(\epsilon_{\beta,\chi}(v_A)) \otimes \delta(\epsilon_{\beta,\chi}(v_b)), \quad b = 1, 2, \dots, B \quad (26)$$

where,  $\otimes$  indicates theLXP operator depends on the XOR operator,  $\epsilon_{\beta,\chi}(\bullet)$  is a phase, and the quantization operator is  $\delta(\bullet)$  that determines the quantized phase code by utilizing multiple phase ranges. Here, LGXP is noted by term  $F(3)$ .

**d) ORB:** ORB [33] is much faster than SURF and scale Invariant Feature Transform (SIFT).ORB extracts meaningful features of images and takes low computational cost when compared to SURF and SIFT. Also, ORB is free when compared to SURF as well as the SIFT algorithm, and is designated as  $F(4)$ .

**e) SURF:** SURF [33] is a speedy version of SIFT and is a local key point descriptor and detector. In the detection of features, SURF utilizes LOG along the box filter algorithm. Moreover, SURF generates good outputs in illumination, rotation, as well as blur when compared with SIFT. Moreover, SURF outperforms SIFT in speed. When compared to features that were retrieved using SIFT, the feature vector length is less. SURF is thus noted by term  $F(5)$ .

**f) Statistical features:** Information from nodule-identified images, such as skewness, standard deviation, variance, kurtosis and mean get extracted.

**i) Mean:** This brings out the brightness of the image, which remains in a consistent manner [34] and consists of a large quantity of bright pixels. The mean is shown here as pixels divided by the whole number of pixels, which are denoted as,

$$S1 = \left( \frac{1}{C \times E} \right) \sum_{\omega=0}^{C-1} \sum_{\xi=0}^{E-1} f(\omega, \xi) \quad (27)$$

where,  $S1$  is mean,  $(C \times E)$  is maximal pixels in the image, and  $(\omega, \xi)$  indicates double axes.

**ii) Variance:** Gray level allocation in the image is termed as variance and if the mean represents grey level variation, then variance gets automatically maximized [34]. It brings out pixel measure in terms of mean and is indicated by,

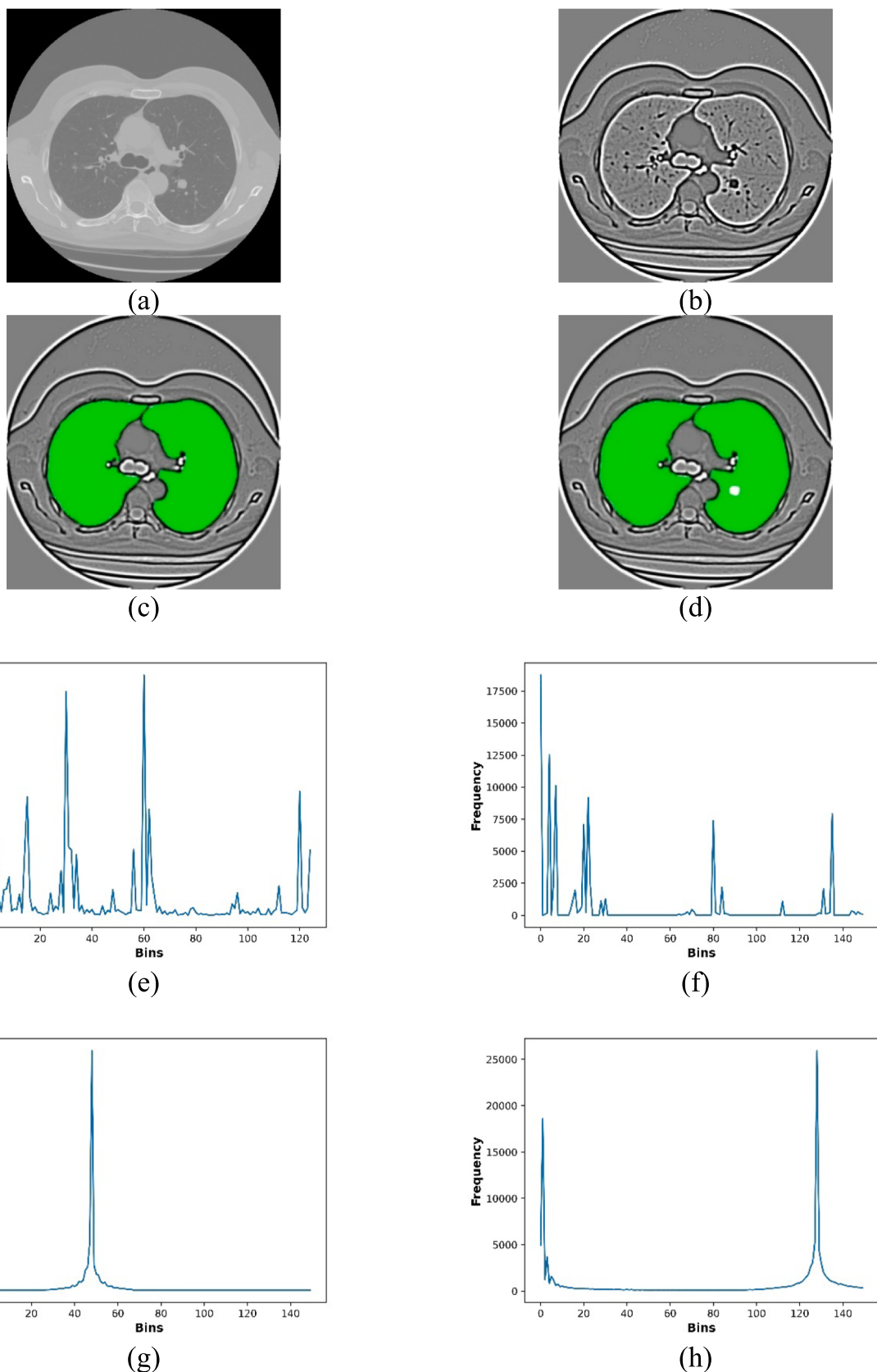


**Fig. 7.** Cancerous CT images experimental results a) input, b) processed, c)lobe segment, d) nodule segment, e) LBP extracted, f) LOOP extracted, g) LGXP extracted, h) ORB extracted and i)SURF extracted images.

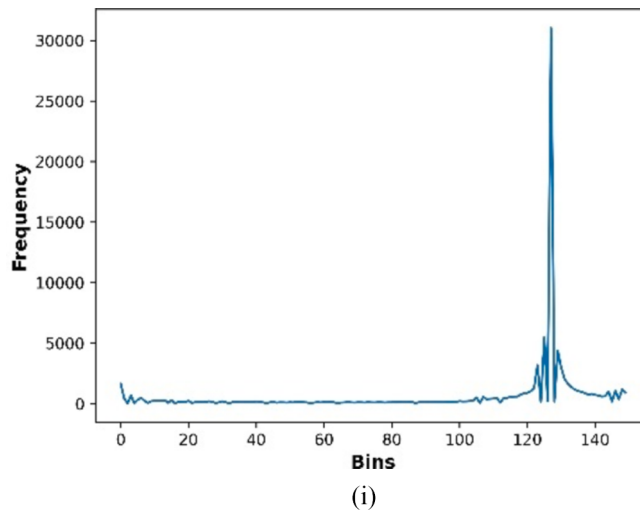


Fig. 7. (continued).

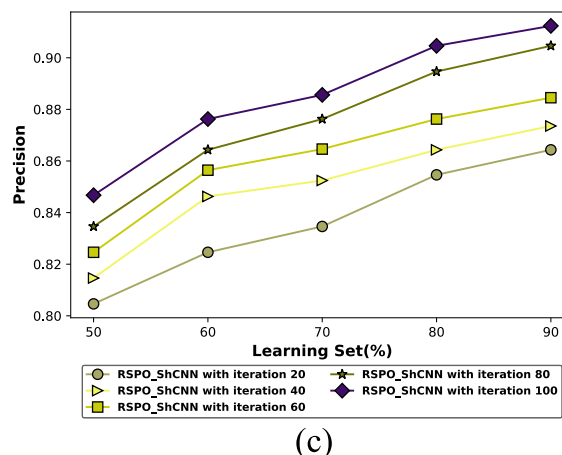
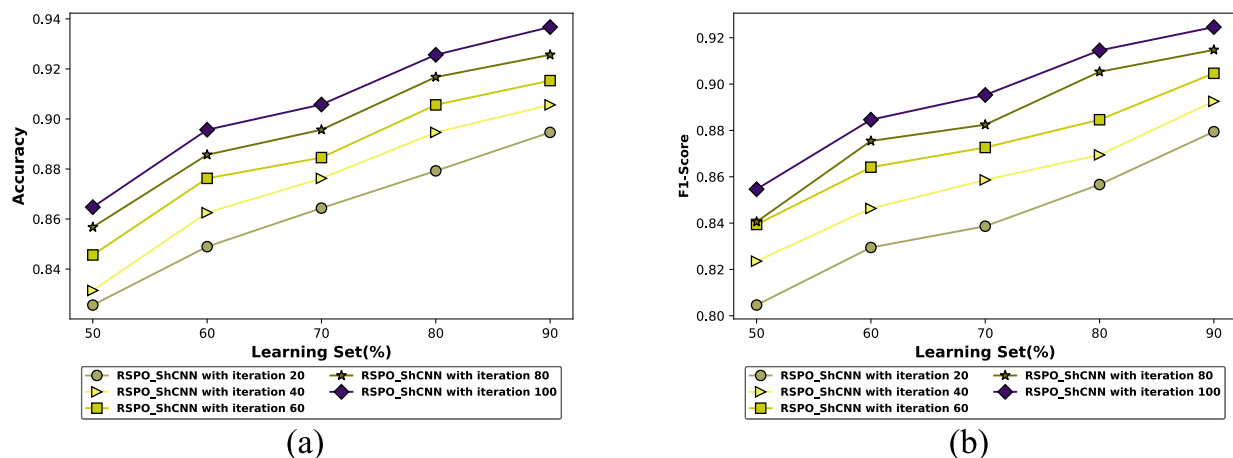


Fig. 8. Performance evaluation for dataset-I, a) Accuracy, b) F-measure, c) Precision.

$$S2 = \left( \frac{1}{C \times E} \right) \sum_{\omega=0}^{C-1} \sum_{\xi=0}^{E-1} (f(\omega, \xi) - S1)^2 \quad (28)$$

where,  $S2$  is variance.

**iii) Kurtosis:** This measures the curve or sharpness in the image, which depends on the distribution of frequency [35] and is designated as  $S3$ .

**iv) Skewness:** Skewness is a variation of symmetry in an image and hence presents asymmetrical variation of the image [35] and is designated as  $S4$ .

**v) Standard deviation:** Standard deviation [36] is the degree of scatter in data with the relationship of mean as well as a measure of dispersion data points from the mean, which is formulated as,

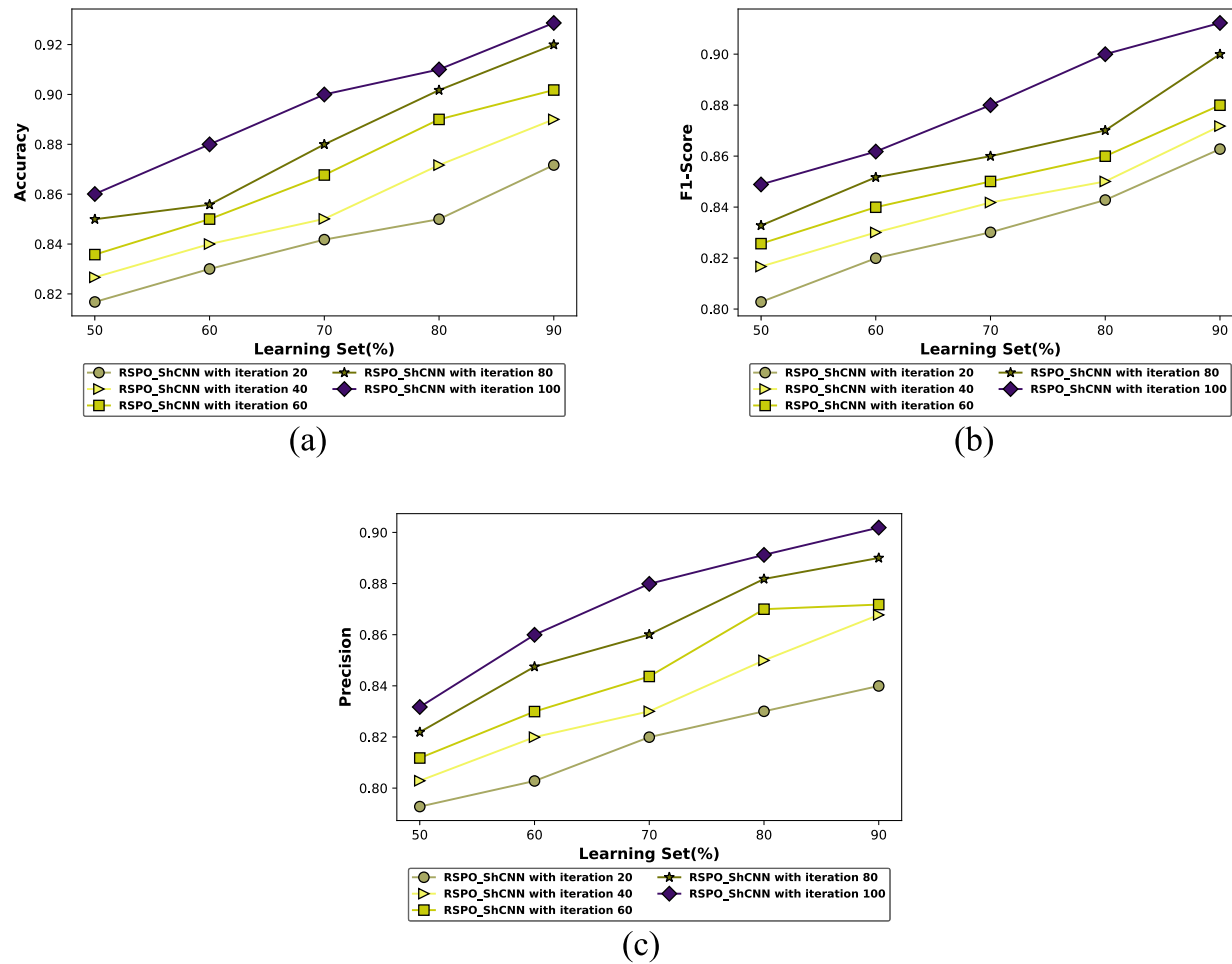


Fig. 9. Performance analysis for dataset-II, a) Accuracy, b) F-measure, c) Precision.

$$S5 = \frac{1}{\mu} \sqrt{\sum_{\omega=1}^{\mu} \sum_{\xi=1}^{\mu} (f(\omega, \xi) - \bar{f})^2} \quad (29)$$

here, rows as well as columns are designated by  $\mu$  and  $S5$  are standard deviations.

Extracted statistical features are indicated by  $F(6) = \{S1, S2, \dots, S5\}$ . Also, the overall extracted features are indicated by below representation,

$$F_c = \{F(1), F(2), \dots, F(6)\} \quad (30)$$

here,  $F_c$  is the total number of extracted features.

### 5.3. Lung cancer detection using Sh CNN

Next to the process of feature extraction, lung cancer is detected by the DL model which is Sh CNN [37]. Here, an extracted feature that is given as input to Sh CNN is indicated as  $F_c$ . This Sh CNN is trained by RSPO, which is a combination of RSO [29] and PO [30]. A full explanation of RSPO is given in section 3.3.2.

#### 5.3.1. ShCNN architecture

ShCNN [37] is a combination of CNN with Shepard interpolation layers that effectively realizes end-to-end trainable Translation Variant Interpolation (TVI) operators in the network. Weighing known pixels based on their spatial distances to processed pixels is done using the Shepard framework. It is given in convolution terms as,

$$G_r = \begin{cases} (H * J)_r / (H * S)_r & \text{if } S_r = 0 \\ J_r & \text{if } S_r = 1 \end{cases} \quad (31)$$

here,  $J$ ,  $G$  is the input and output images,  $r$  and  $S$  represented as index image coordinates and a binary indicator,  $S_r = 0$  is unknown pixel value,  $*$  is an operation on convolution,  $H$  is kernel function with weights with  $S_r = 1$  as well as processing pixel. Element-based division among convolved masks as well as convolved images controls the natural way at which informative pixel is propagated across the regions. A convolutional layer with the Shepard method is generated that allows flexibility, and data-driven kernel design and this layer is indicated as the Shepard interpolation layer, which is indicated as,

$$M_\vartheta^\ell(M^{\ell-1}, S^\ell) = \sigma \left( \sum_{\varpi} \frac{H_{\vartheta\varpi}^\ell * M_{\varpi}^{\ell-1}}{H_{\vartheta\varpi}^\ell * S_{\varpi}^\ell} + P^\ell \right), \quad \ell = 1, 2, 3, \dots \quad (32)$$

here,  $\ell$  is layers index,  $\vartheta$  in  $M_\vartheta^\ell$  is an index of feature maps in  $\ell$ ,  $\varpi$  in  $M_{\varpi}^{\ell-1}$  is an index of feature maps in  $\ell-1$ ,  $M^{\ell-1}$  is input,  $S^\ell$  is the mask of present layer,  $M^{\ell-1}$  is feature maps in the layer  $\ell-1$ ,  $H_{\vartheta\varpi}$  are trainable kernels,  $P$  is bias and  $\sigma$  is non-linearity imposed to network.

Shepard interpolation layer inputs are feature maps or images. Here, the interpolation layer is applied repeatedly for constructing complex interpolation functions having many layers of nonlinearity. The mask is a binary value of 1 for a known area and 0 for a missing area. A similar kernel is used in the image as well as the mask. Mask for layer  $\ell+1$  is generated automatically by the out come of the convolved mask  $H^\ell * S^\ell$ , by zeroing in significant values and then thresholding it. This is indicated as a flexible method for balancing kernel size as well as the net-

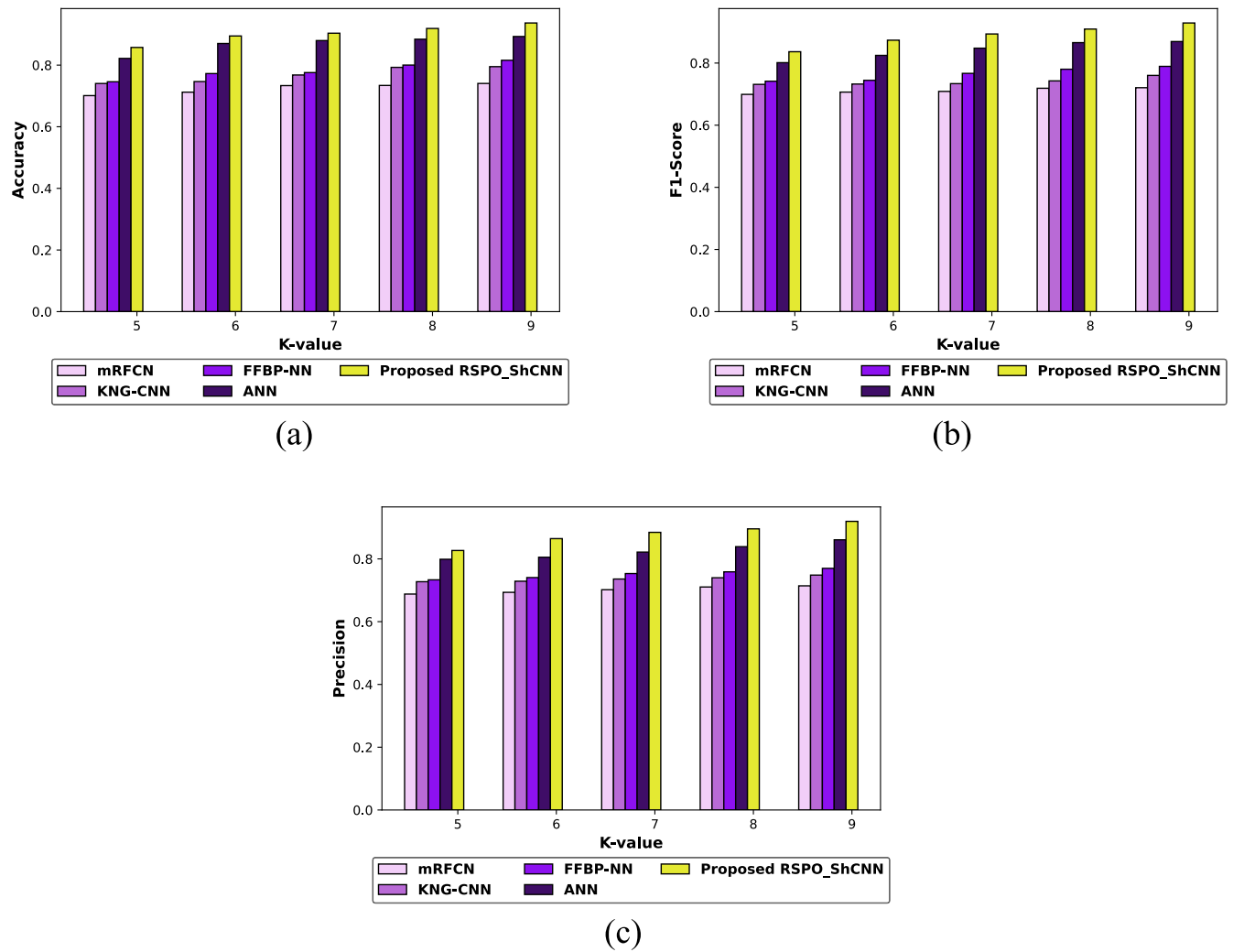


**Fig. 10.** Comparison by altering k-fold for dataset-I, a) Accuracy, b) F-measure, c) Precision.

work's depth. The ShCNN's output is indicated by the term  $Q_c$ . Fig. 3 indicates the architecture of ShCNN which is a combination network of CNN and Shepard interpolation layers.

### 5.3.2. Training of ShCNN by RSPO

ShCNN is trained using a combined optimization technique called RSPO, where section 3.3.2 provides the RSPO algorithmic process. Here, fitness evaluation is changed related to output gained from ShCNN.

#### Evaluation of fitness:

The goal of the fitness evaluation is to achieve optimal results for the training. Here, fitness is evaluated by generated output from ShCNN that is indicated by,

$$Fs_2 = \frac{1}{d} \sum_{c=1}^d [Tar_c^* - Q_c]^2 \quad (33)$$

where,  $Fs_2$  is fitness term based on ShCNN output,  $d$  is total images,  $Q_c$  is output from ShCNN, and  $Tar_c^*$  is targeted output.

According to the fitness equation above, the termination process is carried out until the maximum optimal best answer is obtained.

## 6. Results and discussion

The outcome of RSPO\_ShCNN is elaborated along with experimental outcomes and dataset description. Moreover, the analysis is carried out with performance measures.

### 6.1. Experimental setup

The setup of this experiment for lung cancer detection is done in a Python tool with the LIDC-IDRI dataset [25] and Medical Deepfakes: Lung Cancer dataset [26].

### 6.2. Experimental outcomes

#### i. Experimental results of normal CT images

Experimental images of normal CT images are presented in Fig. 4. The input and processed lung images are indicated in Fig. 4a) and Fig. 4b). The lobe-segmented image, nodule segmented image are represented in Fig. 4c) and Fig. 4d). The LBP extracted, LOOP extracted, LGXP extracted, ORB extracted and SURF extracted images are displayed Fig. 4e), Fig. 4f), Fig. 4g), Fig. 4h) and Fig. 4i).

#### ii. Experimental results of cancerous CT images

Fig. 5 displays the experimental results of cancerous CT images. The input, processed, lobe segmented and nodule segmented images are denoted in Fig. 5a), Fig. 5b), Fig. 5c) and Fig. 5d). The LBP, LOOP, LGXP, ORB and SURF extracted images are illustrated in Fig. 5e), Fig. 5f), Fig. 5g), Fig. 5h) and Fig. 5i).

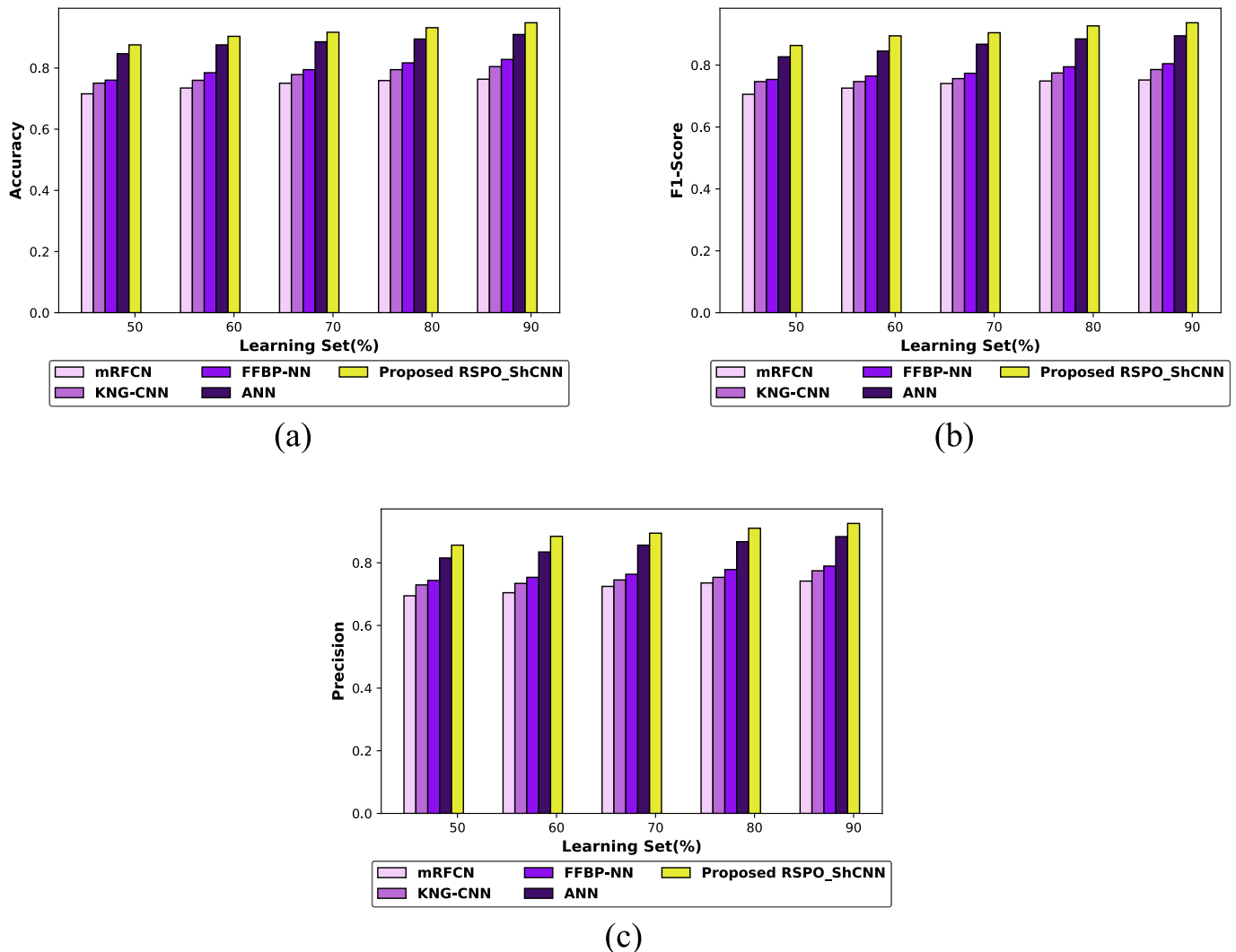


Fig. 11. Comparison by changing learning set for dataset-I, a) Accuracy, b) F-measure, c) Precision.

### 6.2.2. For dataset-II

#### i). Experimental results of normal CT images

Fig. 6 presents the experimental results of normal CT images. The input image is denoted in Fig. 6a). The processed, lobe segmented and nodule segmented images are exhibited in Fig. 6b), Fig. 6c) and Fig. 6d). The LBP extracted image is provided in Fig. 6e). The LOOP extracted, LGXP extracted, ORB extracted and SURF extracted are revealed in Fig. 6f), Fig. 6g), Fig. 6h) as well as Fig. 6i).

#### ii). Experimental results of cancerous CT images

Fig. 7 shows the experimental outcomes of cancerous CT images. The images like input, processed, lobe segmented, nodule segmented, LBP extracted, LOOP extracted, LGXP extracted, ORB extracted and SURF extracted images are provided in Fig. 7a), Fig. 7b), Fig. 7c), Fig. 7d), Fig. 7e), Fig. 7 f), Fig. 7g), Fig. 7h) and Fig. 7i), respectively.

### 6.3. Dataset description

#### 6.3.1. Dataset-I

LIDC-IDRI dataset [25] is the dataset used in this paper. For the purpose of detecting and diagnosing lung cancer, this dataset consists of thoracic computed tomography (CT) scans with marked-up annotated

lesions. It is a global online resource for the creation, training, and evaluation of computer-assisted diagnostic (CAD) methods for lung cancer detection and diagnosis. This 1018-item data set was created in partnership with eight medical imaging companies and seven academic institutions. Four experienced thoracic radiologists in each subject performed a two-step image annotation process on images from a clinical thoracic CT scan and the resulting XML file. It classifies the lesions into 3 types such as nodule  $>or = 3$  mm, nodule  $<3$  mm, and non-nodule  $>or = 3$  mm. Also, it includes the categories such as Lung Cancer, Non-Cancer and Metastatic disease. Furthermore, this dataset size is 133.16 GB.

#### 6.3.2. Dataset-II

Medical Deepfakes: Lung Cancer dataset [26] comprises 100 CT scans divided into two sets: 80 scans and 20 scans. The first 80 scans were used in a blind trial with the radiologists, who were not informed that the scans were tampered with. The remaining 20 scans were used in an open trial, with a radiologist. Each experiment has a CSV table containing the ground truth. Each row in the CSV shows the location and classification of true, false, or removed cancer. Also, it has 4 classes such as True-Benign (TB), False-Benign (FB), True-Malicious (TM) and False-Malicious (FM).

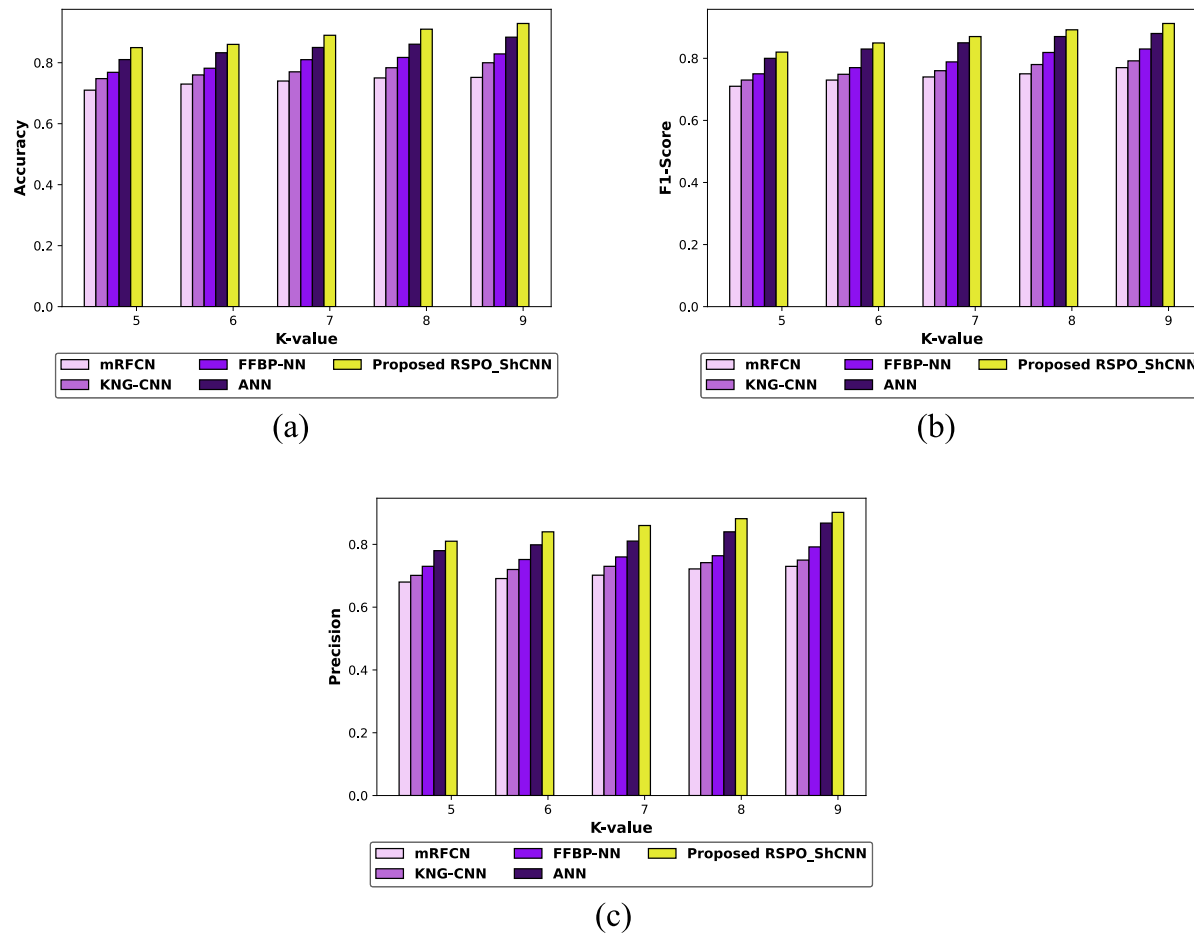


**Fig. 12.** Comparison by altering k-fold for dataset-II, a) Accuracy, b) F-measure, c) Precision.

#### 6.4. Evaluation measures

The metrics used for evaluation are accuracy, F-measure as well as precision that is elaborated on below,

##### 6.4.1. Accuracy

This metric indicates the correct prediction of lung cancer from full infections. By dividing the overall number of cancer predictions by the ratio of clear cancer forecasts, this shows how well the model performed, which is expressed as,

$$A_y = \frac{tr(+) + tr(-)}{tr(+) + tr(-) + fa(+) + fa(-)} \quad (34)$$

here, accuracy is  $A_y$ ,  $tr(+)$  is true positive,  $tr(-)$  is true negative,  $fa(-)$  is false negative, and  $fa(+)$  is false positive.

##### 6.4.2. F-measure

Precision and recall are utilized to measure the F-measure. This is computed to determine the average rate of infectious disease detection and it is indicated as,

$$F_e = \frac{tr(+)}{tr(+) + \frac{1}{2}(fa(+) + fa(-))} \quad (35)$$

where,  $F_e$  is noted for F1-score.

##### 6.4.3. Precision

Accurate data from each summary represents precision, which subsequently illustrates the actual range. This is a real positive fraction to all

positive values that is indicated as,

$$p_{re} = \frac{tr(+)}{tr(+) + fa(+)} \quad (36)$$

here,  $p_{re}$  is precision.

#### 6.5. Performance evaluation

##### 6.5.1. For dataset-I

The performance evaluation of RSPO\_ShCNN by altering the learning set is shown in Fig. 8, where Fig. 8a) suggests accuracy-based performance. Accuracy for RSPO\_ShCNN with iterations 20, 40, 60, 80, and 100 is 0.849, 0.863, 0.876, 0.886, and 0.896, while the learning set is 60. F1-score related performance assessment is indicated in Fig. 8b). While the learning set is 90, F1-score is 0.879, 0.893, 0.905, 0.915, and 0.925 for different iterations as 20, 40, 60, 80, and 100 of RSPO\_ShCNN. Fig. 8c) denotes the precision regarding performance assessment. While learning a set of 70, the precision is 0.886 for RSPO\_ShCNN with iteration 100, whereas RSPO\_ShCNN with iteration 20, 40, 60, and 80 shows precision of 0.835, 0.852, 0.865, and 0.876.

##### 6.5.2. For dataset-II

The performance assessment of RSPO\_ShCNN by adjusting the learning set is depicted in Fig. 9. Fig. 9a) indicates accuracy-based performance evaluation. RSPO\_ShCNN's accuracy at iterations 20, 40, 60, 80, and 100 is 0.817, 0.827, 0.836, 0.850 and 0.860, respectively, with a learning set of 50. Fig. 9b shows an F1-score-related performance analysis. While the learning set is 60, the F1-scores for RSPO\_ShCNN at iterations 20, 40, 60, 80, and 100 are 0.820, 0.830, 0.840, 0.852 and

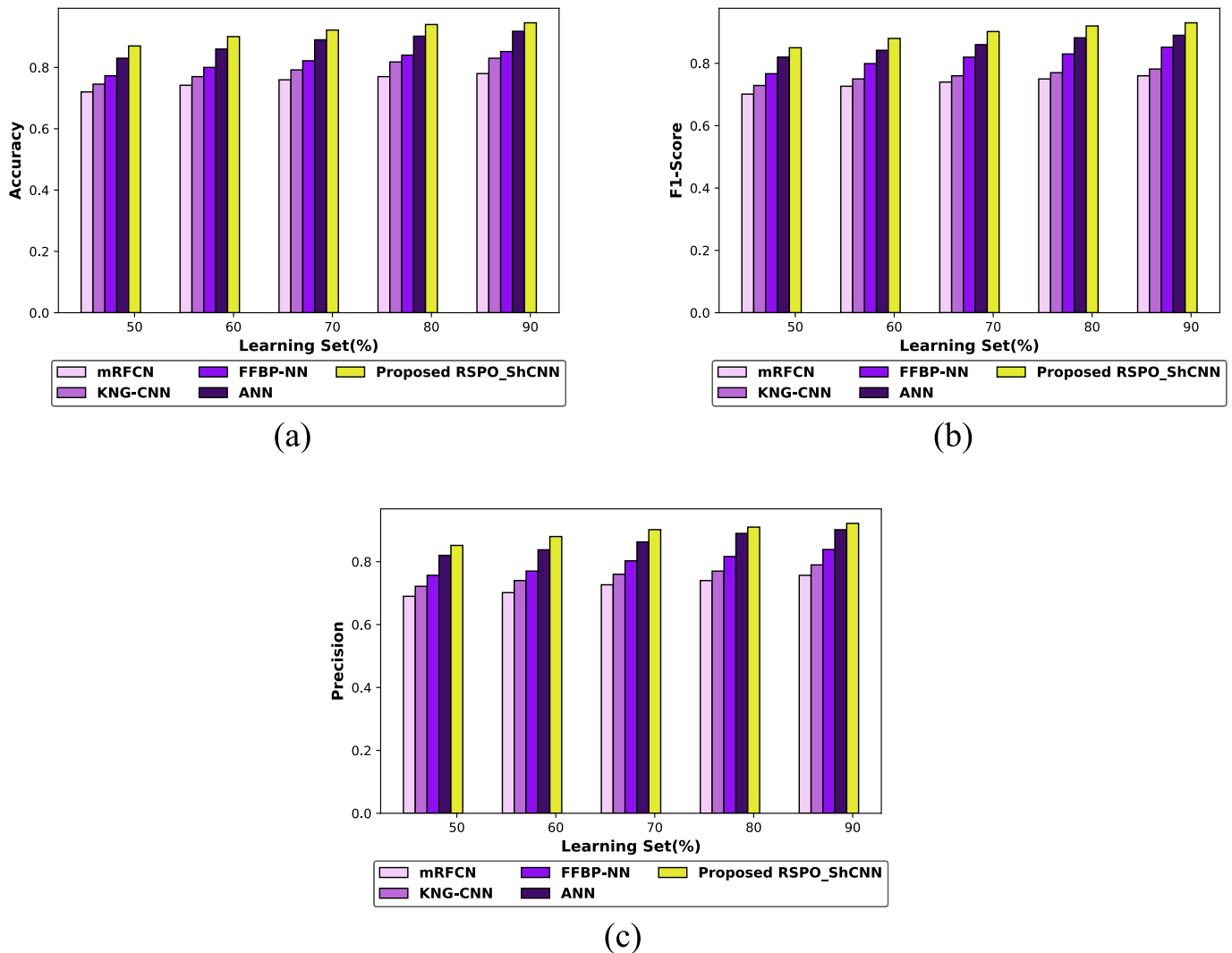


Fig. 13. Comparison by changing learning set for dataset-II, a) Accuracy, b) F-measure, c) Precision.

0.862. Fig. 9c) exhibits the precision-based performance assessment. RSPO ShCNN with iterations 20, 40, 60, 80 and 100 have a precision of 0.820, 0.830, 0.844, 0.860 and 0.880 for considering learning set as 70.

#### 6.6. Comparative methods

The comparative methods used for analysis with RSPO\_ShCNN are mRFCN [3], KNG-CNN [22], FFBP-NN [11], and ANN [7].

#### 6.7. Comparative analysis

Comparative analysis is conducted in two stages: modifying the k-fold and modifying the learning set.

##### 6.7.1. For dataset-I

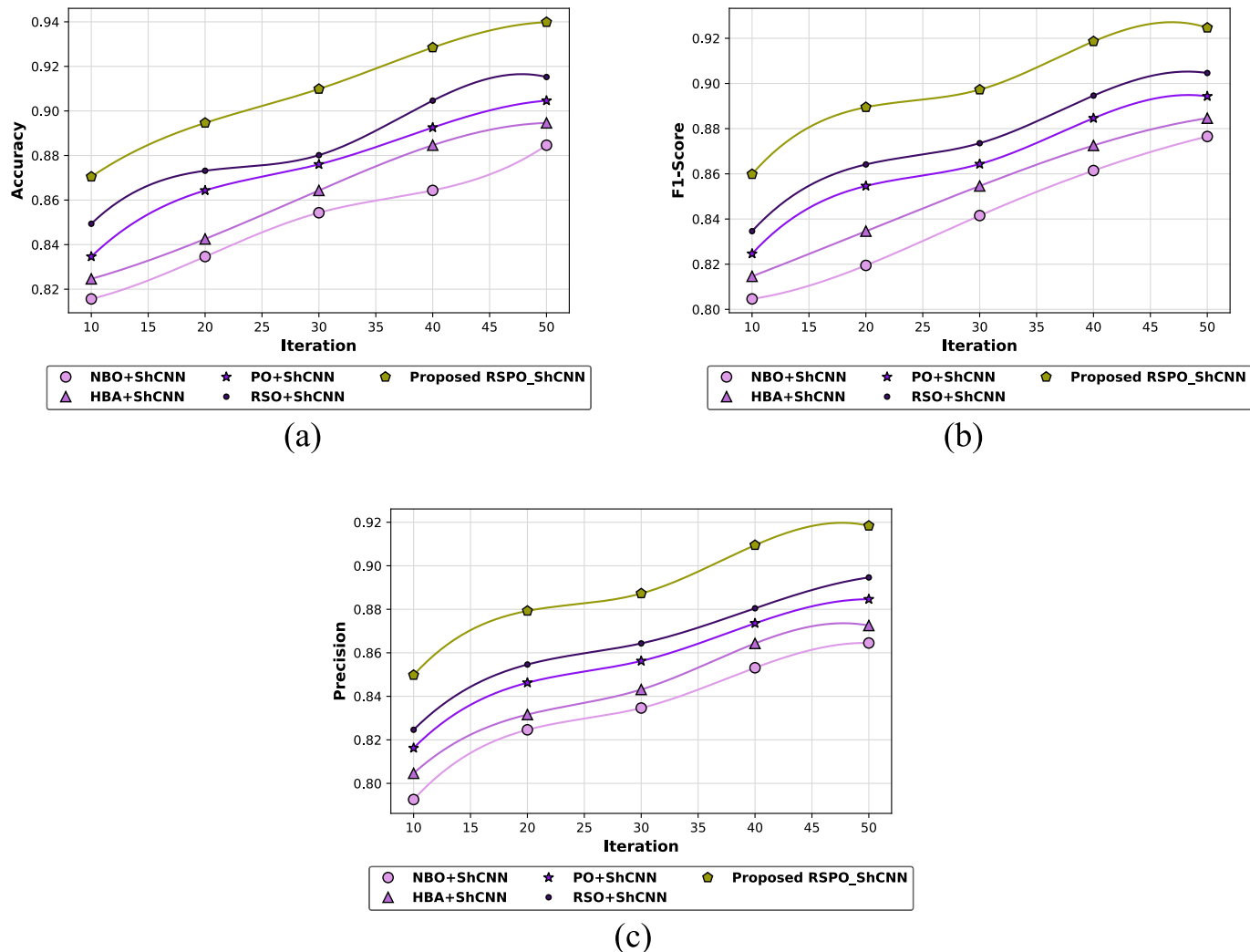
###### i. Comparative analysis by varying k-fold

Fig. 10 indicates the comparison of RSPO\_ShCNN by varying the k-fold value according to dataset-I. Fig. 10a) modifies the k-fold value to show the accuracy-based comparative research. While the k-value is 5, accuracy is 0.701, 0.740, 0.746, 0.822, as well as 0.857 for mRFCN, KNG-CNN, FFBP-NN, ANN, as well as RSPO\_ShCNN. Here, performance improvement is 18.23 %, 13.64 %, 12.99 %, and 4.16 %. Fig. 10b) is an F1-measure based comparison by modifying the k-fold. When the k-

value = 6, the F1 measure of RSPO\_ShCNN is 0.874, wherein other approaches display lesser values of F1 score as 0.707, 0.732, 0.744, and 0.825, with improvement in performance of 19.12 %, 16.16 %, 14.79 %, and 5.60 %. By changing the k-fold value, Fig. 10c) illustrates a comparison study based on precision. For considering k-fold = 8, the precision is high for RSPO\_ShCNN with 0.896, whereas other models show less precision of 0.710, 0.740, 0.759, and 0.839. Here, performance increment is 20.68 %, 17.40 %, 15.28 %, as well as 6.33 %.

###### ii. Comparative analysis by varying learning set

Fig. 11 shows the comparative analysis of RSPO\_ShCNN by changing the learning set with respect to dataset-I. The accuracy-related comparative analysis by changing the learning set value is represented in Fig. 11a). For the 90 % learning set, the accuracy of RSPO\_ShCNN is high at 0.948, whereas other methods has the accuracy of 0.763, 0.805, 0.828, and 0.909, with enhancement in performance of 19.45 %, 15.12 %, 12.66 %, and 4.05 %. Fig. 11b) is F1-measure enabled comparative assessment by changing the learning set. While considering the learning set as 80, F1-measure is 0.749, 0.775, 0.795, 0.885, and 0.927 for mRFCN, KNG-CNN, FFBP-NN, ANN, and RSPO\_ShCNN. Here, performance improvement is 19.23 %, 16.41 %, 14.26 %, and 4.55 %. Fig. 11c) portrays the comparison of precision based examination of RSPO\_ShCNN by modifying the learning set. For considering learning percentage is 90, the RSPO\_ShCNN has a higher precision of 0.926,



**Fig. 14.** Algorithmic evaluation by altering iteration for dataset-I, a) Accuracy, b) F-measure, c) Precision.

whereas other models show lesser precision of 0.742, 0.775, 0.789, as well as 0.884. It gives the 19.87 %, 16.32 %, 14.71 %, and 4.55 % performance enhancement.

#### 6.7.2. For dataset-II

##### i. Comparative assessment based on varying k-fold

Fig. 12 provides a comparison of RSPO\_ShCNN with different k-fold values depend on dataset-II. Accuracy-based comparative study is demonstrated in Fig. 12a). While the k-value is 5, the accuracy is 0.710 for mRFCN, 0.748 for KNG-CNN, 0.768 for FFBP-NN and 0.810 for ANN, and 0.850 for RSPO\_ShCNN. In this instance, the RSPO\_ShCNN has improved performance by 16.47 %, 12 %, 6.65 %, and 4.71 %. Fig. 12b) depicts an F1-measure-based comparison that modifies the k-fold. For considering k-value = 6, the F1 measure for RSPO\_ShCNN is 0.849, whereas other methods have the F1 scores of 0.730, 0.749, 0.770 and 0.830. The RSPO\_ShCNN results in performance improvements of 14.02 %, 11.78 %, 9.31 %, and 2.24 %. Fig. 12c) illustrates the precision-based comparative research. The RSPO\_ShCNN has a high precision of 0.860, and the previous models like mRFCN, KNG-CNN, FFBP-NN as well as ANN achieves the precisions of 0.702, 0.730, 0.760 and 0.810, for considering the k-value of 7.

##### ii. Comparative assessment based on varying learning set

Fig. 13 denotes the comparative study of RSPO\_ShCNN depending on varying learning sets by using dataset-II. Fig. 13a demonstrates the accuracy-related comparison analysis using different learning set values. With the 90 % learning set, RSPO\_ShCNN offers an accuracy of 0.946. The accuracy values obtained by the mRFCN are 0.780, KNG-CNN is 0.830, FFBP-NN is 0.852 and ANN is 0.918. Fig. 13b) displays an F1-measure-based comparison evaluation with a changed learning set. For taking learning set = 80, mRFCN, KNG-CNN, FFBP-NN, ANN, and RSPO\_ShCNN have F1-measures of 0.750, 0.770, 0.830, 0.882 and 0.920. Here, the analysis depicts that the RSPO\_ShCNN is 18.47 %, 16.30 %, 9.78 %, and 4.13 % superior to mRFCN, KNG-CNN, FFBP-NN and ANN. In Fig. 13c), a precision-based comparison of RSPO\_ShCNN is shown for various learning sets. At a learning percentage of 70, RSPO\_ShCNN achieves a precision of 0.902. Moreover, the other models have the precision scores of 0.727, 0.760, 0.803 and 0.863.

#### 6.8. Algorithmic methods

Various algorithmic methods used in this paper compared with RSPO\_ShCNN are NBO [38] + ShCNN, HBA [39] + ShCNN, PO [30] + ShCNN, and RSO [37] + ShCNN.

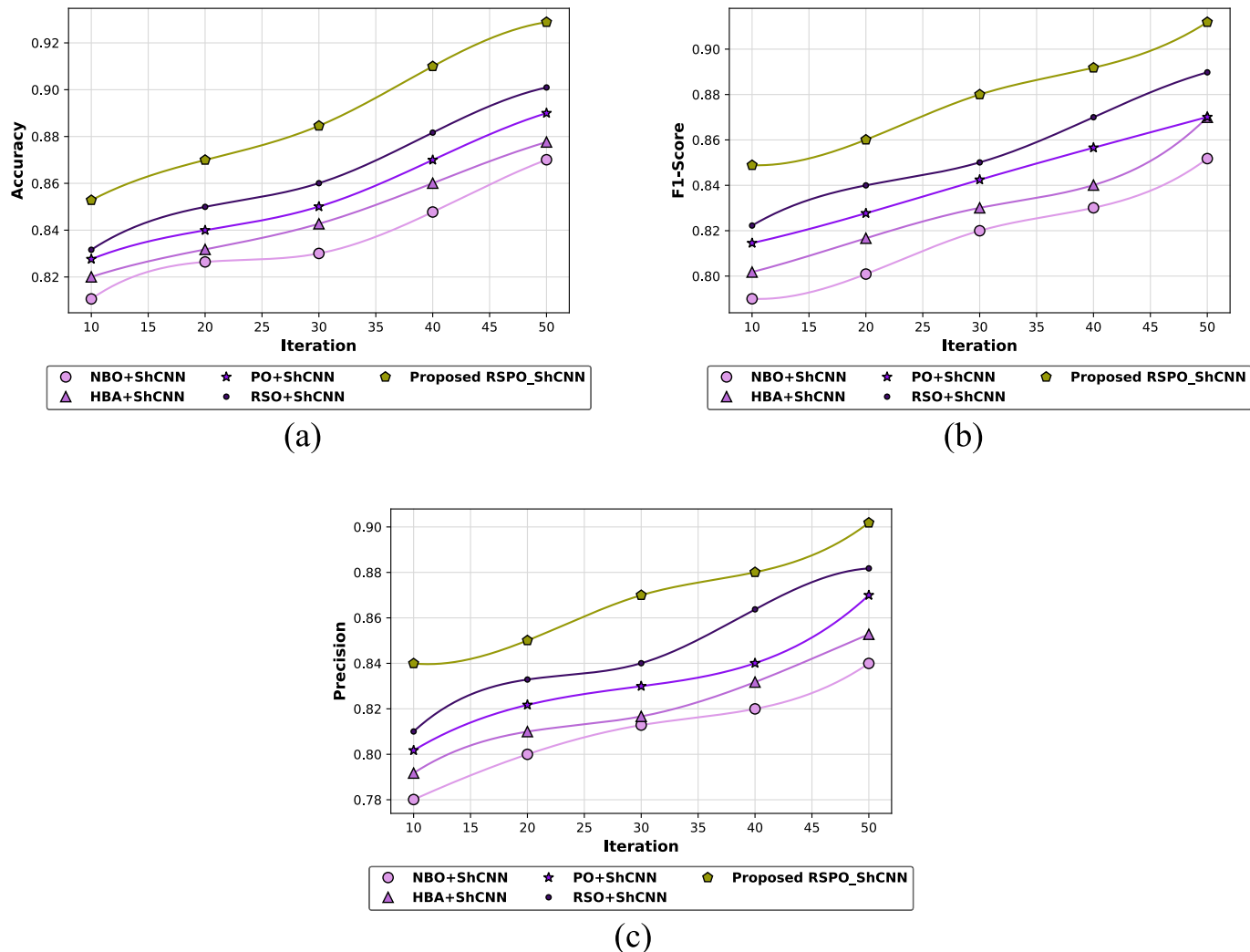


**Fig. 15.** Algorithmic evaluation by altering iteration for dataset-II, a) Accuracy, b) F-measure, c) Precision.

**Table 2**  
Comparative discussion of RSPO\_ShCNN.

Classification	Metrics / Methods	mRFCN	KNG-CNN	FFBP-NN	ANN	Proposed RSPO_ShCNN
<b>For dataset-I</b>						
Training data = 90 %	Accuracy	76.3 %	80.5 %	82.8 %	90.9 %	<b>94.8 %</b>
	F-measure	75.2 %	78.6 %	80.5 %	89.5 %	<b>93.7 %</b>
	Precision	74.2 %	77.5 %	78.9 %	88.4 %	<b>92.6 %</b>
K-fold = 9	Accuracy	74.0 %	79.5 %	81.6 %	89.3 %	93.7 %
	F-measure	72.1 %	76.0 %	78.9 %	86.9 %	92.9 %
	Precision	71.4 %	74.8 %	77.0 %	86.1 %	92.0 %
<b>For dataset-II</b>						
Training data = 90 %	Accuracy	78.0 %	83.0 %	85.2 %	91.8 %	94.6 %
	F-measure	76.0 %	78.2 %	85.2 %	89.0 %	93.0 %
	Precision	75.7 %	79.0 %	83.9 %	90.2 %	92.2 %
K-fold = 9	Accuracy	75.2 %	80.0 %	82.9 %	88.4 %	92.9 %
	F-measure	77.0 %	79.2 %	83.0 %	88.0 %	91.2 %
	Precision	73.0 %	75.0 %	79.2 %	86.8 %	90.2 %

## 6.9. Algorithmic assessment

### 6.9.1. For dataset-I

Fig. 14 shows the RSPO\_ShCNN's algorithmic evaluation by altering iteration. Fig. 8a offers algorithmic analysis based on accuracy. When iteration is 30, accuracy is 0.854, 0.864, 0.876, 0.880, as well as 0.910 for NBO + ShCNN, HBA + ShCNN, PO + ShCNN, RSO + ShCNN and

RSPO\_ShCNN, with performance improvement of 6.10 %, 5.00 %, 3.72 %, and 3.26 %. Fig. 14b) is the F1-measure based algorithmic assessment. When iteration is 40, then the F1 value is high of 0.919 for RSPO\_ShCNN, but prevailing methods give low F1 values of 0.861, 0.873, 0.885, and 0.895, with 6.22 %, 5.01 %, 3.70 %, as well as 2.61 % performance improvement. Fig. 14c) is a precision based algorithmic evaluation. When the iteration is 10, the precision is 0.793, 0.805,

**Table 3**  
Analysis based on computational time and memory usage.

	mRFCN	KNG-CNN	FFBP-NN	ANN	Proposed RSPO_ShCNN
<b>For dataset-I</b>					
<i>Computational time (s)</i>	73.35	65.83	61.28	47.59	39.59
<i>Memory usage (MB)</i>	43.9	42.7	42.3	36.5	35.6
<b>For dataset-II</b>					
<i>Computational time (s)</i>	74.96	67.77	56.57	48.60	37.97
<i>Memory usage (MB)</i>	45.6	43	41.6	38.2	36.2

0.816, 0.825, and 0.850 for NBO + ShCNN, HBA + ShCNN, PO + ShCNN, RSO + ShCNN and RSPO\_ShCNN, with enhancement in performance of 6.73 %, 5.31 %, 3.95 %, and 2.96 %.

#### 6.9.2. For dataset-II

Fig. 15 displays the algorithmic evaluation of RSPO\_ShCNN with varying iterations by using dataset-II. In Fig. 8a), the accuracy-based analysis is shown. At 50 iterations, the accuracy values are 0.870 for NBO+ShCNN, 0.878 for HBA+ShCNN, 0.890 for PO+ShCNN, 0.901 for RSO+ShCNN, and 0.929 for RSPO\_ShCNN. This proves that RSPO\_ShCNN is 6.35 %, 5.49 %, 4.20 %, and 3.01 % higher than NBO+ShCNN, HBA+ShCNN, PO+ShCNN and RSO + ShCNN. Fig. 15b) demonstrates the RSPO\_ShCNN's algorithmic evaluation with respect to the F1-measure. The F1-measure of RSPO\_ShCNN, NBO+ShCNN, HBA+ShCNN, PO+ShCNN and RSO+ShCNN is 0.892, 0.830, 0.840, 0.857 and 0.870, for considering iteration = 40. It proves that RSPO\_ShCNN has attained higher F1-measure by 6.95 %, 5.83 %, 3.92 %, as well as 2.47 % than previous methods. Fig. 15c) illustrates an algorithmic evaluation based on precision. When considering the iteration as 20, the precision for NBO+ShCNN, HBA+ShCNN, PO+ShCNN, RSO+ShCNN, and RSPO\_ShCNN is 0.800, 0.810, 0.822, 0.833 and 0.850, with performance enhancement of 5.88 %, 4.71 %, 3.29 %, and 2 %.

#### 6.10. Comparative discussion

A comparative discussion of RSPO\_ShCNN with other models is enumerated in Table 2. From Table 2, accuracy is high at 0.948 and this is due to the utilization of PSPNet for lung lobe segmentation. Also, RSPO\_ShCNN shows a higher F1 measure of 0.937 and this is because of the grid-based scheme used for nodule identification. Moreover, precision is superior to 0.926 and this is because of ShCNN used for lung cancer detection that is trained by RSPO. The higher values of metrics like accuracy, F1 measure, and precision are attained by varying training data.

#### 6.11. Analysis based on computational time and memory usage

Table 3 illustrates the analysis of RSPO\_ShCNN based on computational time and memory usage. Computational time describes the amount of time an algorithm takes to complete the task. Also, the memory usage refers to the amount of memory consumed by the algorithm during its execution. Here, the invented RSPO\_ShCNN achieves a lower computational time of 37.97 s and lower memory usage of 35.6 MB, compared to traditional methods, such as mRFCN, KNG-CNN, FFBP-NN and ANN.

#### 6.12. Application and significance of this study

By accurately segmenting lung lobes, it helps doctors to make treatment plans specific to the affected areas, improving the effectiveness. It is used in clinical decision-making by aiding radiologists in

identifying lung nodules with high accuracy. It identifies lung cancer at a potentially curable stage and also helps in risk assessment and treatment planning. It effectively reduces the lung cancer mortality rates, especially in high-risk populations. Furthermore, it provides precise localization of lung abnormalities, leading to more accurate diagnoses and treatments. Also, the proposed RSPO\_ShCNN is used in the automated analysis systems in the hospitals and automated screening programs.

#### 6.13. Hypothesis, limitations and future work of this research

The hypothesis of this paper is to develop two novel networks such as RSPO\_PSPNet for lung lobe segmentation and RSPO\_ShCNN for lung cancer detection. The main limitation of the invented model is it heavily relies on the quality and diversity of training data. This model does not have the integration of clinical metadata, like patient history, symptoms, and other relevant data. Future research will focus on rigorously validating the model and addressing these risks. In future, this model can be used for other applications like detecting cancer in other body parts with an accurate rate of prediction. Also, it will be allowed for real-time segmentation in clinical settings to enhance computational efficiency. Moreover, own datasets will be considered in future for experimentation.

#### 7. Conclusion

In this work, RSPO\_PSPNet is invented for lung lobe segmentation and RSPO\_ShCNN is proposed for lung cancer detection. Moreover, the RSPO is an integration of an RSO and PO. First, the Laplacian filter is used for image pre-processing. Then, the PSPNet is used for lung lobe segmentation, which is trained by a newly formed RSPO. Subsequently, a grid-based approach is employed to identify the nodules, after which features are extracted. Next, the ShCNN detects lung cancer, which is trained by the RSPO. Moreover, the RSPO\_ShCNN achieves an accuracy of 0.948, an F-measure of 0.926 and a precision of 0.937. These superior results are obtained due to the effective integration of RSO and PO. This combination results in faster convergence, improved optimization, and better feature extraction, which in turn leads to higher performance in lung cancer detection and lung lobe segmentation.

#### CRediT authorship contribution statement

**N. Velmurugan:** Conceptualization, Methodology, Validation, Writing - Original Draft, Writing - Review & Editing. **R. Rajeswari:** Writing – review & editing. **Satuluri Naganjaneyulu:** Writing – review & editing. **A. Anupama:** Writing – review & editing.

#### Declaration of competing interest

The authors declare that they have no known competing financial interests or personal relationships that could have appeared to influence the work reported in this paper.

#### Data availability

No data was used for the research described in the article.

#### References

- [1] S.A. Althubiti, S. Paul, R. Mohanty, S.N. Mohanty, F. Alenezi, K. Polat, Ensemble learning framework with GLCM texture extraction for early detection of lung cancer on CT images, Comput. Math. Methods Med. 2022 (1) (2022) 2733965.
- [2] K.D. Miller, L. Nogueira, A.B. Mariotto, J.H. Rowland, K.R. Yabroff, C.M. Alfano, A. Jemal, J.L. Kramer, R.L. Siegel, Cancer treatment and survivorship statistics, CA: Cancer J. Clin. 69 (2019) 5363–5385.
- [3] A. Masood, B. Sheng, P. Yang, P. Li, H. Li, J. Kim, D.D. Feng, Automated decision support system for lung cancer detection and classification via enhanced RFCN with multilayer fusion RPN, IEEE Trans. Ind. Inf. 16 (12) (2020) 7791–7801.

- [4] N.A. Wani, R. Kumar, J. Bedi, DeepExplainer: An interpretable deep learning based approach for lung cancer detection using explainable artificial intelligence, *Comput. Methods Programs Biomed.* 1 (243) (2024) 107879.
- [5] B.A. Skourt, A. El Hassani, A. Majda, Lung CT image segmentation using deep neural networks, *Procedia Comput. Sci.* 1 (127) (2018) 109–113.
- [6] C.W. Bong, H.Y. Lam, A.T. Khader, H. Kamarulzaman, Adaptive multi-objective archive-based hybrid scatter search for segmentation in lung computed tomography imaging, *Eng. Optim.* 44 (3) (2012) 327–350.
- [7] B.K. Veronica, An effective neural network model for lung nodule detection in CT images with optimal fuzzy model, *Multimed. Tools Appl.* 79 (19) (2020) 14291–14311.
- [8] S. Balasubramaniam, S. Kadry, K.S. Kumar, Osprey Gannet optimization enabled CNN based Transfer learning for optic disc detection and cardiovascular risk prediction using retinal fundus images, *Biomed. Signal Process. Control* 1 (93) (2024) 106177.
- [9] S. Kadry, R.K. Dhanaraj, S.K. K, C. Manthiramoorthy, Res-Unet based blood vessel segmentation and cardio vascular disease prediction using chronological chef-based optimization algorithm based deep residual network from retinal fundus images, *Multimed. Tools Appl.* 20 (2024) 1–30.
- [10] S.L. Lee, A.Z. Kouzani, E.J. Hu, Automated detection of lung nodules in computed tomography images: a review, *Mach. Vis. Appl.* 23 (2012) 151–163.
- [11] P. Nanglia, A.N. Mahajan, D.S. Rathee, S. Kumar, Lung cancer classification using feed forward back propagation neural network for CT images, *Int. J. Med. Eng. Inf.* 12 (5) (2020) 447–456.
- [12] Q. Li, Recent progress in computer-aided diagnosis of lung nodules on thin-section CT, *Comput. Med. Imaging Graph.* 31 (4–5) (2007) 248–257.
- [13] Y. Rajan Baby, V.K. Ramayyan Sumathy, Kernel-based Bayesian clustering of computed tomography images for lung nodule segmentation, *IET Image Proc.* 14 (5) (2020) 890–900.
- [14] S. Park, S.M. Lee, S. Kim, J.G. Lee, S. Choi, K.H. Do, J.B. Seo, Volume doubling times of lung adenocarcinomas: correlation with predominant histologic subtypes and prognosis, *Radiology* 295 (3) (2020) 703–712.
- [15] A.Z. Foeady, S.R. Riqmawatin, D.C. Novitasari, Lung cancer classification based on CT scan image by applying FCM segmentation and neural network technique, *Telkomnika (Telecommunication Computing Electronics and Control)*. 19 (4) (2021) 1284–1290.
- [16] L. Tiwari, R. Raja, V. Awasthi, R. Miri, G.R. Sinha, M.H. Alkinani, K. Polat, Detection of lung nodule and cancer using novel Mask-3 FCM and TWEDLNN algorithms, *Measurement* 1 (172) (2021) 108882.
- [17] S. Balasubramaniam, M. Arishma, R.K. Dhanaraj, A Comprehensive Exploration of Artificial Intelligence Methods for COVID-19 Diagnosis, *EAI Endorsed Trans. Pervasive Health Technol.* 21 (2024) 10.
- [18] S. Balasubramaniam, A. Prasanth, K.S. Kumar, V. Kavitha, Medical Image Analysis Based on Deep Learning Approach for Early Diagnosis of Diseases, in: *Deep Learning for Smart Healthcare*, Auerbach Publications, 2024, pp. 54–75.
- [19] A. Choudhury, S. Balasubramaniam, A.P. Kumar, S.N. Kumar, PSSO: Political squirrel search optimizer-driven deep learning for severity level detection and classification of lung cancer, *Int. J. Inf. Technol. Decis. Mak.* 31 (2023) 1–34.
- [20] J. Long, E. Shelhamer, T. Darrell, Fully convolutional networks for semantic segmentation, *IEEE*, 2015, pp. 3431–3440.
- [21] H. Zunair, A.B. Hamza, Sharp U-Net: Depthwise convolutional network for biomedical image segmentation, *Comput. Biol. Med.* 1 (136) (2021) 104699.
- [22] S.R. Jena, S.T. George, Morphological feature extraction and KNG-CNN classification of CT images for early lung cancer detection, *Int. J. Imaging Syst. Technol.* 30 (4) (2020) 1324–1336.
- [23] M. Navaneethakrishnan, M.V. Anand, G. Vasavi, V.V. Rani, Deep Fuzzy SegNet-based lung nodule segmentation and optimized deep learning for lung cancer detection, *Pattern Anal. Appl.* 26 (3) (2023) 1143–1159.
- [24] L.J. Crasta, R. Neema, A.R. Pais, A novel deep learning architecture for lung cancer detection and diagnosis from computed tomography image analysis, *Healthcare Anal.* 1 (5) (2024) 100316.
- [25] LIDC-IDRI dataset is taken from "<https://wiki.cancerimagingarchive.net/display/Public/LIDC-IDRI>", accessed on April 2023.
- [26] Medical Deepfakes: Lung Cancer is taken from "<https://www.kaggle.com/datasets/ymlirsky/medical-deepfakes-lung-cancer>", accessed in 2020.
- [27] H. Kong, H.C. Akakin, S.E. Sarma, A generalized Laplacian of Gaussian filter for blob detection and its applications, *IEEE Trans. Cybern.* 43 (6) (2013) 1719–1733.
- [28] H. Zhao, J. Shi, X. Qi, X. Wang, J. Jia, Pyramid scene parsing network, *IEEE*, 2017, pp. 2881–2890.
- [29] G. Dhiman, M. Garg, A. Nagar, V. Kumar, M. Dehghani, A novel algorithm for global optimization: rat swarm optimizer, *J. Ambient Intell. Hum. Comput.* 12 (2021) 8457–8482.
- [30] Q. Askari, I. Younas, M. Saeed, Political Optimizer: A novel socio-inspired meta-heuristic for global optimization, *Knowl.-Based Syst.* 11 (195) (2020) 105709.
- [31] D. NarainPonraj, E. Christy, G. Aneesha, G. Susmitha, M. Sharu, Analysis of LBP and LOOP based textural feature extraction for the classification of CT Lung images, *IEEE*, 2018, pp. 309–312.
- [32] S. Xie, S. Shan, X. Chen, J. Chen, Fusing local patterns of gabor magnitude and phase for face recognition, *IEEE Trans. Image Process.* 19 (5) (2010) 1349–1361.
- [33] M. Bansal, M. Kumar, M. Kumar, 2D object recognition: a comparative analysis of SIFT, SURF and ORB feature descriptors, *Multimed. Tools Appl.* 80 (12) (2021) 18839–18857.
- [34] M.O. Khairandish, M. Sharma, V. Jain, J.M. Chatterjee, N.Z. Jhanjhi, A hybrid CNN-SVM threshold segmentation approach for tumor detection and classification of MRI brain images, *ibrm*. 43 (4) (2022) 290–299.
- [35] D.J. Hemanth, EEG signal based modified Kohonen neural networks for classification of human mental emotions, *J. Artif. Intell. Syst.* 2 (1) (2020) 1–3.
- [36] A.C. Reddy, Evaluation of surface roughness using image processing technique, *InInt. Conf. Syst. Cybern. Inform.* (2004) 571–573.
- [37] J.S. Ren, L. Xu, Q. Yan, W. Sun, Shepard convolutional neural networks, *Adv. Neural Inf. Proces. Syst.* 28 (2015).
- [38] M. Chahardoli, N.O. Eragli, S. Nazari, Namib beetle optimization algorithm: a new meta-heuristic method for feature selection and dimension reduction, *Concurrency Comput. Pract. Exper.* 34 (1) (2022) e6524.
- [39] F.A. Hashim, E.H. Houssein, K. Hussain, M.S. Mabrouk, W. Al-Atabany, Honey Badger Algorithm: New metaheuristic algorithm for solving optimization problems, *Math. Comput. Simul.* 1 (192) (2022) 84–110.